Tailored heat treatments to enhance performance in additive manufactured HAYNES® 282® superalloy

MTLA 39 (2025) 102334

Contents lists available at ScienceDirect

Materialia

journal homepage: www.elsevier.com/locate/mtla

Full Length Article

Tailored heat treatments to enhance performance in additive manufactured HAYNES® 282® superalloy

Abdul Shaafi Shaikh [a,b,*], Emil Eriksson [c], Magnus Hörnqvist Colliander [c], Kevin Minet-Lallemand [b], Eduard Hryha [a]

[a] Chalmers University of Technology, Department of Industrial and Materials Science, Rännvägen 2A, Gothenburg 41296, Sweden
[b] Electro Optical Systems Finland Oy, Lemminkäisenkatu 36, 20520 Turku, Finland
[c] Chalmers University of Technology, Department of Physics, Kemigården 1, Gothenburg 41296, Sweden

ARTICLE INFO

Keywords:
Additive manufacturing
Powder bed fusion – laser beam
Haynes 282
Heat treatment
Creep

ABSTRACT

While additive manufacturing (AM) has made considerable strides towards industrialization in recent years, its application to superalloys is still limited. This is in part because superalloys manufactured by AM often show anisotropic mechanical properties and creep performance inferior to their cast or wrought counterparts. HAYNES® 282® (282 alloy) is one such alloy which originated in wrought form but has been rapidly adopted in AM. However, AM 282 alloy currently shows deficient high temperature performance relative to wrought 282 alloy, especially when conventional heat treatment is applied to the AM alloy. This study aims to understand how AM and specifically powder bed fusion – laser beam (PBF-LB) processed 282 alloy compares to wrought 282 alloy in terms of microstructure and mechanical properties, and how these can be improved by different heat treatment regimes. 282 alloy manufactured by PBF-LB was subjected to three different solution heat treatments: the conventional solution heat treatment at 1135 °C, a high temperature solution treatment at 1250 °C, and hot isostatic pressing (HIP) at 1250 °C. All materials were double aged at 1010 °C and 788 °C. Mechanical testing showed that solution treatments at 1250 °C reduced anisotropy relative to the typical 1135 °C solution treatment, especially at high temperature. Most significantly, creep rupture life at 927 °C and 89 MPa was doubled (reaching >300 h compared to 115 h for wrought), and minimum creep rate was reduced by an order of magnitude even compared to the wrought counterpart. The improved high temperature mechanical performance was correlated with more equiaxed and coarse grains, tortuous grain boundaries, frequent twins, and specific grain boundary microstructure. The study highlights the critical role of grain structure in high temperature performance, and demonstrates the necessity of tailored heat treatments for enhancing the properties of AM superalloys[1].

1. Introduction

Superalloys as high temperature materials are irreplaceable in the aerospace and power-generation industries. The application of additive manufacturing (AM) technologies to superalloys has promised to bring engineers and designers greater freedom and flexibility in the use of these materials. AM also carries benefits in manufacturing lead time, light-weighting, and buy-to-fly ratios for the production of high-performance engineering components, including those made from superalloys. However, the number of superalloys available for AM remains severely limited, owing to the historically poor weldability and formability of many superalloys. Nevertheless, the potential advantages to the aerospace and energy industries from increased adoption of various superalloys in AM remain highly desirable.

HAYNES® 282® (henceforth referred to as 282 alloy) was introduced in 2005 as a new wrought nickel-base superalloy with an excellent balance of strength, high temperature stability, and formability. It was designed to out-perform and partially replace legacy wrought superalloys such as Waspaloy and Inconel 718 which have limitations either in fabricability or service temperature. 282 alloy in wrought form has since been adopted for various components in aero-engines and industrial gas turbines, among other applications [1].

* Corresponding author.
E-mail address: abdulsh@chalmers.se (A.S. Shaikh).

[1] "Haynes" and "282" are registered trademarks of Haynes International, Inc., Kokomo, Indiana, USA.

https://doi.org/10.1016/j.mtla.2025.102334
Received 11 June 2024; Accepted 2 January 2025
Available online 3 January 2025

The use of 282 alloy in AM has been investigated extensively in recent years. Various AM technologies have been utilized, including powder bed fusion - electron beam (PBF-EB), directed energy deposition (DED), and Powder Bed Fusion – Laser Beam (PBF-LB) [2–4]. Overall, 282 alloy has been shown to have good processability in these fusion based AM techniques and the resulting mechanical properties are described as generally comparable to the wrought material. However, the high temperature performance, especially creep performance of the alloy, has not yet been well evaluated. AM superalloys are known to be severely anisotropic in terms of creep and high temperature tensile performance, and typically underperform their cast or wrought counterparts [5,6]. Properties in orientations perpendicular to the build direction are known to be relatively poor, and the same has been observed for PBF-LB processed 282 alloy [2].

The heat treatment of PBF-LB 282 alloy up until now has mainly been performed according to the solution treatment (at 1135 °C) and ageing heat treatments (at 1010 °C and 788 °C) defined for the wrought alloy. However, recent results have shown that use of a solution heat treatment at 1250 °C can help to reduce the anisotropy and improve high temperature mechanical properties, though the mechanisms behind the effects are not well understood [7,8]. The use of Hot Isostatic Pressing (HIP) is also of interest, as this process is often applied to critical components for safety purposes, and several different HIP treatments have been applied to PBF-LB 282 alloy with varying outcomes [9–11]. This study therefore aims to understand how different heat treatment regimes can influence the microstructure and mechanical performance of PBF-LB 282 alloy. It is also recognized, however, that the wrought material, due to its familiar and standardized properties [12], remains a benchmark in terms of performance. The wrought material is therefore included in the test matrix of this work as a reference.

2. Materials and methods

2.1. Sample manufacturing

Test samples of PBF-LB 282 alloy were manufactured in an EOS M290 PBF-LB system (Electro Optical Systems GmbH, Krailling, Germany) which has a 250 mm x 250 mm x 325 mm building volume. The powder used for the PBF-LB process was gas atomized EOS NickelAlloy HAYNES® 282® powder supplied by EOS. PBF-LB processing was performed using the 40 μm layer thickness process parameters from the "Haynes282_040_080_CoreM291" process parameter set from EOS.

Sample geometries included cuboids of dimensions 15 mm x 15 mm x 18 mm for metallographic examination as well as horizontally and vertically oriented mechanical test blanks of length ≈ 80 mm and diameter of ≈ 11 mm. A bandsaw was used to remove the samples from the building platform.

Wrought material was supplied by Haynes International Inc. in the form of 15.9 mm thick plate in the mill annealed condition. Blanks for mechanical testing were cut from this plate in the long transverse direction using a metallographic cutting saw. An overview of the sample geometries and section orientations is given in Fig. 1.

2.2. Heat treatments

Heat treatments according to the test matrix in Table 1 were performed. Four different heat treatment conditions for 282 alloy were studied. The conditions Sol_1135, Sol_1250, and HIP_1250 used PBF-LB 282 alloy. Samples for Sol_1135 were given a solution treatment of 1135 °C for 2 hrs, following the typical solution treatment used for wrought material and defined by Haynes International Inc and relevant material standard specifications [1,13,14]. Samples for Sol_1250 were subjected to a solution treatment of 1250 °C for 2 hrs, intended to induce static

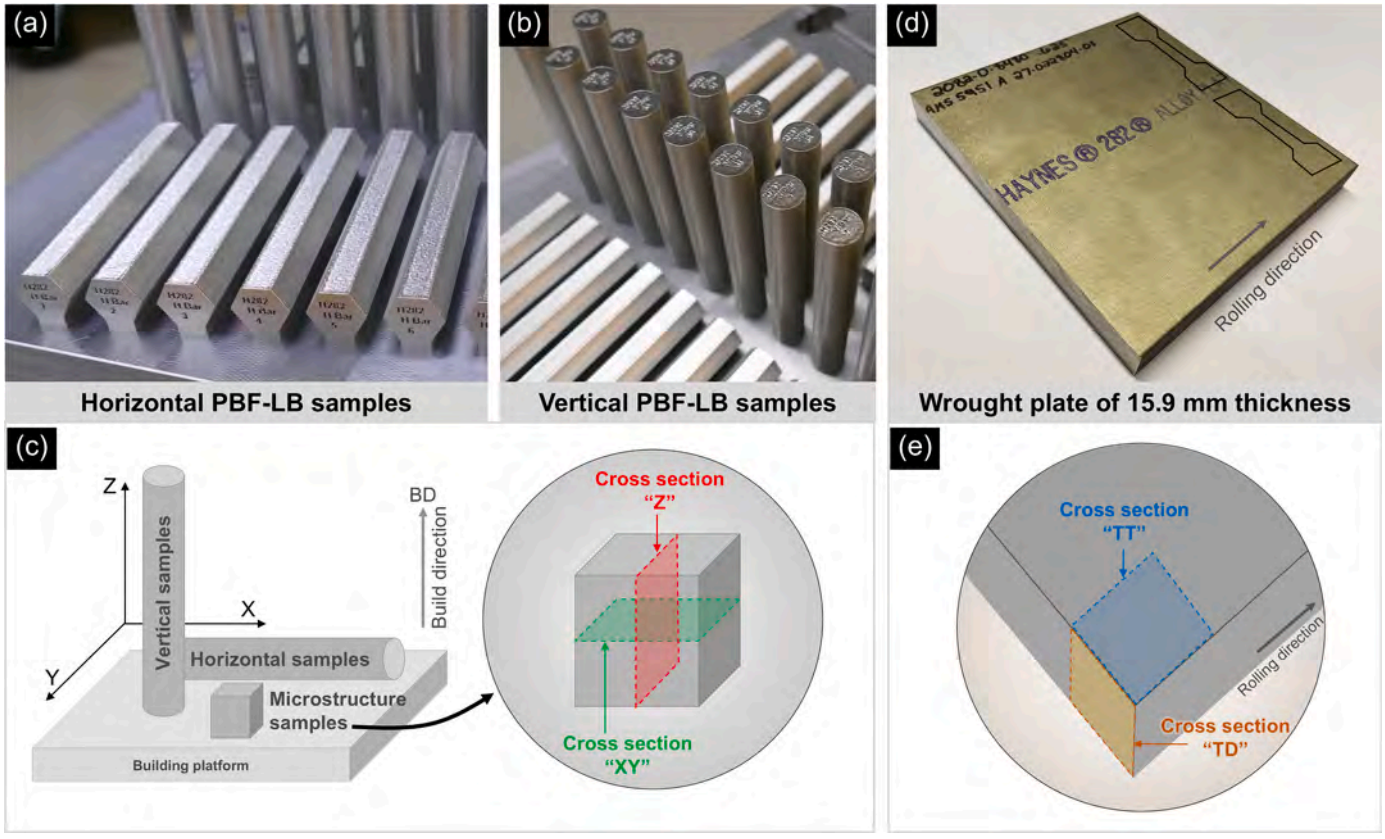

Fig. 1. (a) PBF-LB 282 alloy samples built horizontally; (b) PBF-LB 282 alloy samples built vertically; (c) sample and cross-section orientations for PBF-LB 282 alloy; (d) wrought 282 alloy plate; (e) sample and cross-section orientations for wrought 282 alloy.

Table 1
Definition of the processing and heat treatment history of the studied material conditions.

Condition	Processing	Solution treatment	Ageing
Sol_1135	PBF-LB	1135 °C / 2 hrs, forced Ar cooling	1010 °C / 2 hrs, forced Ar cooling + 788 °C / 8 hrs, forced Ar cooling
Sol_1250	PBF-LB	1250 °C / 2 hrs, forced Ar cooling	- " -
HIP_1250	PBF-LB	HIP at 1250 °C / 4 hrs and 100 MPa, rapid Ar cooling	- " -
Wrought	Plate, 15.9 mm thickness	Mill annealed (between 1121 °C and 1177 °C + water quench) performed by Haynes Intl	- " -

recrystallization and grain growth in the microstructure. Samples for HIP_1250 were given a HIP treatment at 1250 °C for 4 hrs under 100 MPa in Ar, intended to heal defects from the PBF-LB processing, as well as to produce a recrystallized and coarse grained microstructure. The HIP included a rapid quench to room temperature.

Wrought material (condition referred to as "Wrought") was included in the test matrix as a benchmark. The material was received in mill-annealed condition, and no additional solutionising was done after receipt.

Samples for all conditions were subjected to the same two-step ageing heat treatment, which is prescribed by standard material specifications and recommended by Haynes International, with the intent to exclude the ageing as a variable in the text matrix.

The conventional heat treatments were performed in a TAV H4-S type industrial vacuum furnace (TAV Vacuum Furnaces SPA, Caravaggio BG, Italy). Pressurized Ar gas was used for the cooling steps. A schematic representation of the different heat treatments is given in Fig. 2.

Chemical composition analysis of the PBF-LB and wrought material was performed after full heat treatment. Contents of C and S were analysed by the combustion method according to ASTM E1019, contents of N and O were analysed by the fusion method according to ASTM E1019, and all other elements were analysed by Inductively Coupled Plasma Optical Emission Spectroscopy according to ASTM E2594.

2.3. Metallographic preparation and evaluation

Given the known anisotropy of PBF-LB manufactured metallic materials, cross-sections of PBF-LB 282 alloy both parallel to building direction (Z) and perpendicular to building direction (XY) were prepared (see Fig. 1). Samples were cut by a metallographic saw and mounted in Struers' "Polyfast" conductive resin. Progressive grinding with SiC papers up to P1000 was followed by progressive polishing to 1 μm with diamond paste. Samples for Electron Backscattered Diffraction (EBSD) analysis were further polished with 0.25 μm fumed silica until relief of grain boundaries was visible optically. Samples for scanning electron microscope (SEM) analysis were electrolytically etched with 10 % oxalic acid to reveal the microstructure.

Optical microscopy was performed on an Olympus GX51 optical microscope. SEM analysis was mainly performed on a Zeiss GeminiSEM 450 microscope, with a Bruker FlatQuad detector being used for Energy Dispersive X-ray Spectroscopy (EDX) analysis. Additional SEM analysis was performed on Thermo-Fischer Scientific Apreo 2 SEM. EBSD analysis was performed on a Tescan GAIA3 FIB-SEM with Oxford NordLys II EBSD detector, and the ATEX [15] and Oxford Aztec Crystal software were used for analysis of EBSD data. A Tescan VEGA3 SEM was used for fractography.

2.4. Mechanical testing

The blanks for room temperature tensile testing were machined into a cylindrical tensile specimen shape with a gauge length of 25.4 mm and 4.70 mm gauge diameter. Room temperature tensile tests were performed in crosshead control with strain rate equivalent to 2.5×10^{-4} s^{-1} until yield followed by 2×10^{-3} s^{-1} until fracture. Tensile test blanks for elevated temperature testing were also machined to threaded cylindrical specimens with a 5 mm gauge diameter and 25 mm gauge length. Testing was done in crosshead control with an equivalent strain rate of 2.5×10^{-4} s^{-1} until yield followed by 1.4×10^{-3} s^{-1} until fracture. The values of yield strength, ultimate tensile strength, elongation after fracture, and area reduction were determined according to the ISO 6892–1 and ISO 6892–2 standards for tensile testing. A minimum of two samples were tested per condition.

Samples for creep and stress rupture testing were machined into cylindrical specimens with gauge diameter of 6 mm and parallel length of 30 mm, with elongations being measured over a gauge length of 24 mm. Creep strain tests and stress rupture tests were performed according to ASTM E139 with constant tensile load.

3. Results

3.1. Chemical composition

The results from the chemical analysis (Table 2) showed that the

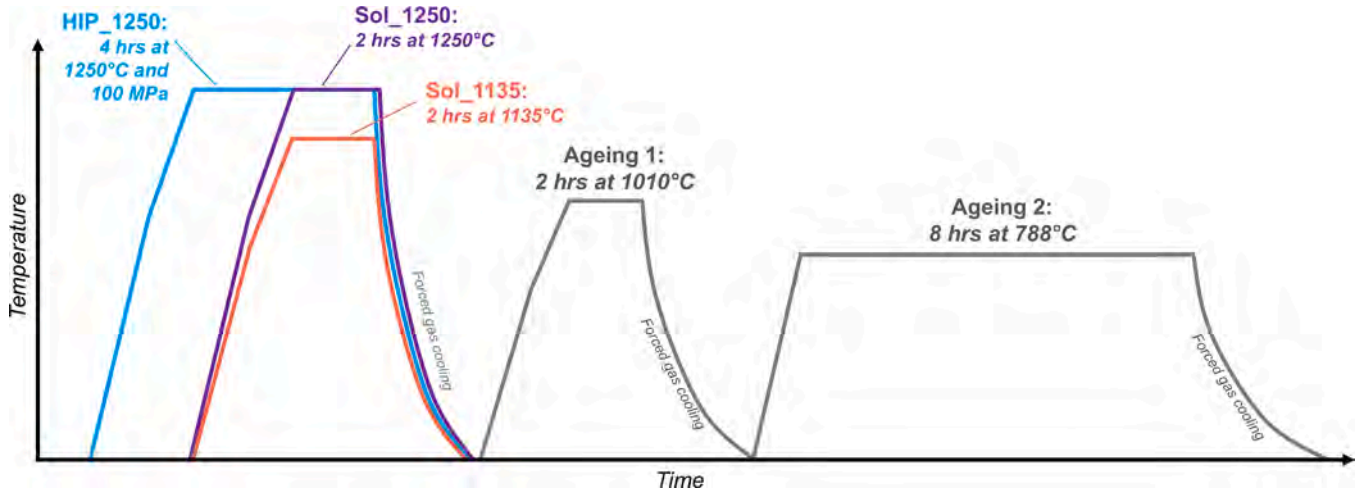

Fig. 2. Schematic representation of heat treatments applied to PBF-LB 282 alloy.

Table 2
Chemical composition of the PBF-LB manufactured and wrought forms of 282 alloy.

wt.%	Ni	Cr	Co	Mo	Ti	Al	C	B	Zr	O	N	S	Fe	Mn	Si
PBF-LB	Balance	18.9	9.6	8.8	2.17	1.50	0.063	0.0054	< 0.0005	0.010	0.011	< 0.002	0.032	0.009	< 0.015
Wrought	Balance	19.2	9.6	8.4	2.05	1.53	0.057	0.0061	0.0005	< 0.002	0.005	< 0.002	0.951	0.072	0.039

PBF-LB and wrought 282 alloy materials were very similar in composition in terms of alloying elements. The wrought material was, however, found to be much lower in O and N content than the PBF-LB material, which is expected given the multiple melting and refining steps that are typically employed in production of cast and wrought superalloys [16, 17]. Importantly the S content was found to be below the detection limit of 20 ppm by weight in both forms of the alloy, a result which agrees well with previously reported measurements of impurities in 282 alloy [17]. Compared to the PBF-LB alloy, slightly higher amounts of Fe, Mn, and Si were measured in the wrought alloy. Note that analyses were performed on solid material after full heat treatment so as to be relevant for understanding of the microstructures and mechanical performance.

3.2. Microstructure

Low magnification micrographs of the four material conditions are presented in Fig. 3. All materials manufactured by PBF-LB were found to contain some small fraction of porosity. The PBF-LB conditions without HIP, that is Sol_1135 and Sol_1250, showed defect area fractions in the range of 0.018 % to 0.030 % as measured by image analysis. The defects were pores and lack of fusion defects and typically <20 μm in size. The largest defects in a roughly 10 mm x 10 mm region of interest were found to be up to around 100 μm in diameter in a sample of Sol_1135. Defect analysis of the PBF-LB sample after HIP and ageing (HIP_1250 condition) showed a notable reduction in defect count, defect area fraction, defect density, as well as maximum defect size. Detailed defect analysis results for the three PBF-LB material conditions are given in Table 3.

While no porosity was observed in the wrought material (as expected) the occurrence of coarse carbides in the microstructure was noted. These carbides were tens of microns in size with blocky morphology and arranged in bands or stringers along the rolling

Table 3
Defect distributions in the PBF-LB 282 alloy samples in different conditions. ROI = Region of interest.

Condition	Section	Defect-% [%]	Defect count (total in ROI)	ROI Area [mm^2]	Max. Defect dia [μm]	Defect density [1/mm^2]
Sol_1135	Z	0.018	651	107.5	39.9	6.05
	XY	0.020	540	108.5	102.9	4.98
Sol_1250	Z	0.030	897	115.1	75.5	7.79
	XY	0.026	620	113.3	69.5	5.47
HIP_1250	Z	0.002	156	113.1	23.2	1.38
	XY	0.002	161	120.0	12.3	1.34

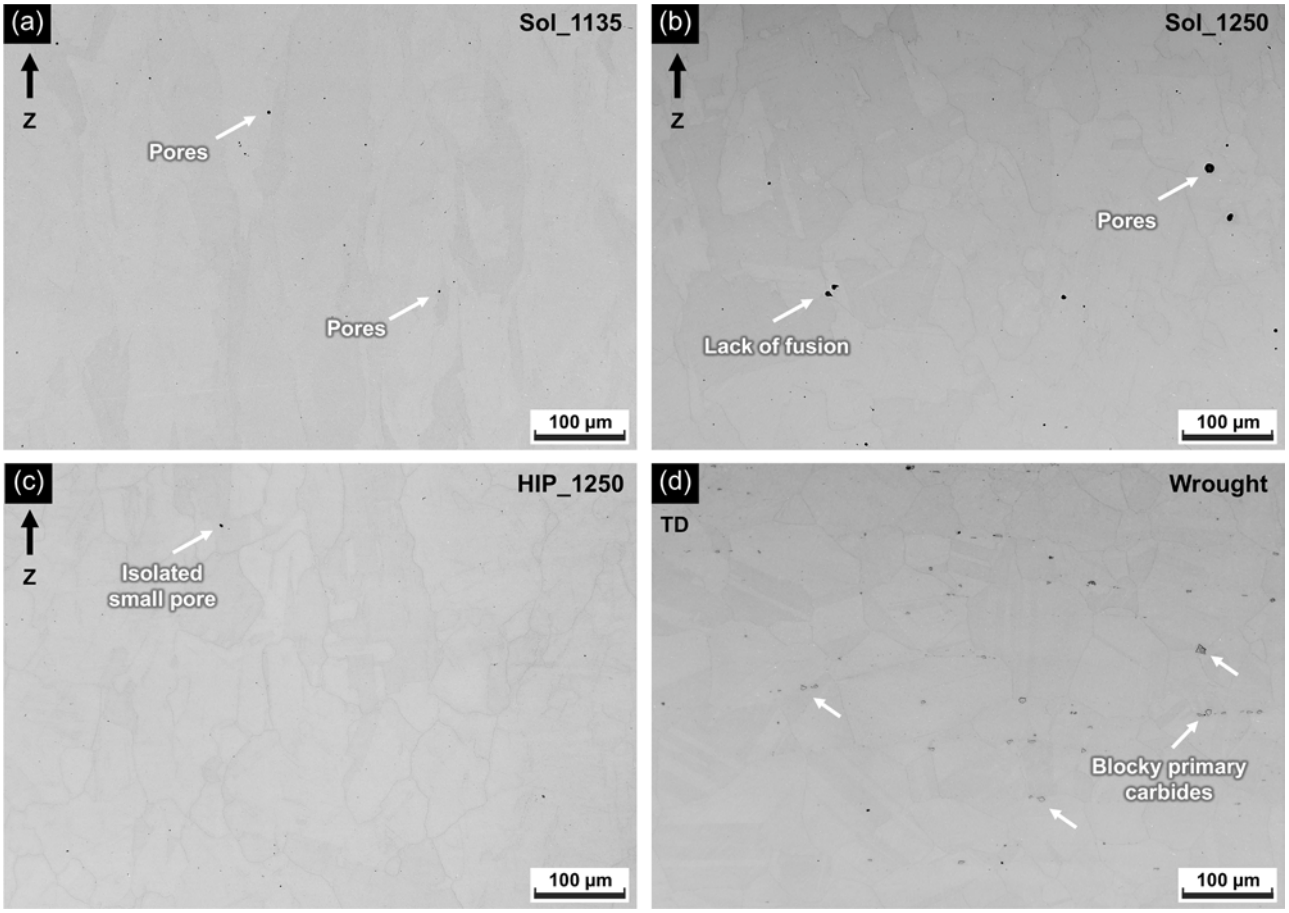

Fig. 3. Optical micrographs of the material in different heat treatment conditions, with (a) Sol_1135; (b) Sol_1250; (c) HIP_1250; (d) Wrought.

direction. Such microstructural features are often observed in cast and wrought austenitic materials and have been commonly reported in wrought 282 alloy [18,19].

EBSD analysis results of the grain structure of the four conditions in two orientations each are shown in Fig. 4. Data on grain sizes, aspect ratios, and grain boundary characteristics are shown in Fig. 5 and Table 4. Misorientation for grain determination was set at 10°, the grain sizes were converted to equivalent circle diameter (ECD), and parent grains were used for size analysis, i.e. twin boundaries were not considered. The grain size and aspect ratio data for AM materials are often widely distributed, and a simple mean may be misrepresentative, therefore box-and-whisker plots showing median (Q2), first quartile (Q1) and third quartile (Q3), as well as mean have been plotted and can be seen in Fig. 5. Additionally, EBSD orientation maps with inverse pole figure (IPF) representation can be found in the Supplementary Material Figure S1.

The Sol_1135 condition was characterized by a columnar grain structure, as shown in Fig. 4 (a-b). Fine elongated grains with very high aspect ratio (median of 2.8 as shown in Fig. 5(b)) were observed in the Z cross-section parallel to the building direction. Perpendicular to the building direction the grains had a smaller aspect ratio (median of 1.9), with a median grain size of only 9 μm ECD. The Z and XY cross-sections considered together show that the grains in three dimensions have an elongated ellipsoidal morphology, typical of PBF-LB processed materials. Twin boundaries, shown in red, and identified as having misorientation of around 60±3.5°, were not observed in the Sol_1135 samples.

Compared to Sol_1135, the Sol_1250 (see Fig. 4(c) and (d)) samples showed coarser grains, with median grain sizes of 47 μm ECD and 32 μm ECD in XY and Z cross-sections respectively. Median grain aspect ratios were <2 in both orientations, however looking at Fig. 4(c) and (d) it is apparent that the grains were not spherical or elliptical, but rather irregular in shape. As shown in Fig. 4(e) and (f), the HIP_1250 condition presented a higher fraction of coarser grains in the Z cross-section (see Fig. 4(e)), resulting in Q3 grain size of 159 μm ECD (see Fig. 5(a)), but this condition otherwise presented similar features to the Sol_1250 condition.

The Wrought condition, as shown in Fig. 4(g) and (h), exhibited a grain structure typical of rolled plate or sheet product forms, having regular polygonal grains. Median grain sizes were measured to be 43 μm ECD in the TT cross-section and 29 μm in the TD cross-section. The grain size distributions in both cross-sections were similar except that the TD cross-section showed many very small grains around the carbide stringers (see Figure S2 in Supplementary Material) which lowered the median value relative to the TT cross-section. The aspect ratios of the Wrought samples were measured to be a median of 1.6 in both orientations and showed the narrowest distribution of all conditions, having interquartile range of only 0.7 in both orientations.

Compared to the other conditions, Sol_1135 produced the narrowest distribution of grain sizes, having an interquartile range of only 13 μm ECD in the XY cross-section. The Sol_1250 and HIP_1250 grain sizes were more widely distributed, with some grains being very large and others relatively small. However, even the Q1 ECD grain sizes of Sol_1250 and HIP_1250 were larger than the median grain sizes of Sol_1135 in either orientation. With regard to aspect ratios, the Sol_1250, HIP_1250, and Wrought conditions produced narrow distributions of aspect ratios whereas the Sol_1135 condition produced grain structure with more widely distributed aspect ratios. The larger grain sizes and smaller aspect ratios provide evidence that substantial grain growth occurred in the Sol_1250 and HIP_1250 conditions during the post-PBF-LB heat treatment.

Large fractions of twin boundaries were observed in the Sol_1250 and HIP_1250 conditions, and twins were small and widely distributed, as seen in Fig. 4(c) to (h) and Table 4. Grains in the Wrought condition also showed frequent twinning, however, the twin boundaries tended to cut across whole grains from grain boundary to grain boundary, unlike those in the Sol_1250 and HIP_1250 conditions.

The different heat treatment conditions also showed pronounced differences in texture. Grains in the Sol_1135 condition showed strong

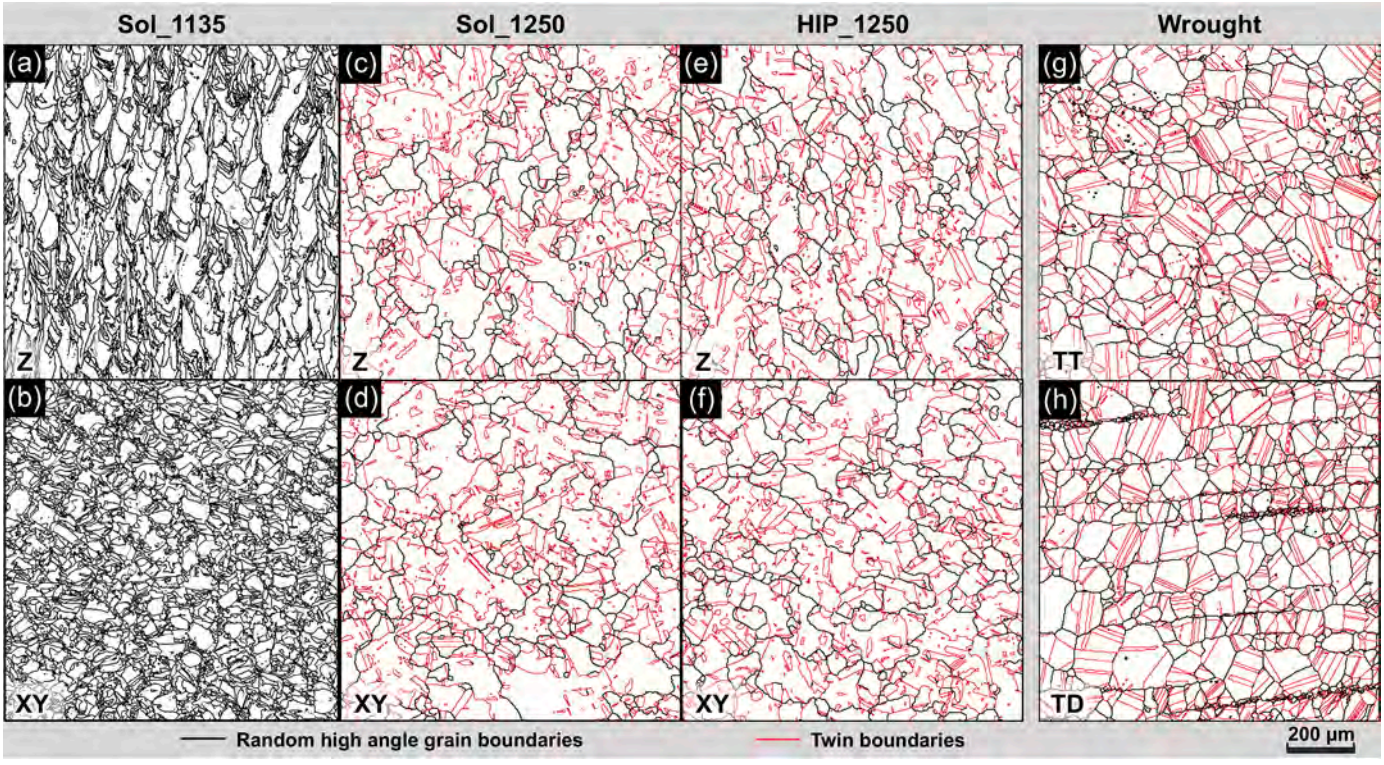

Fig. 4. Grain structure of samples from different conditions in two cross-section orientations, from EBSD measurements, with (a)-(b) Sol_1135; (c)-(d) Sol_1250; (e)-(f) HIP_1250; (g)-(h) Wrought. Random high angle grain boundaries are coloured black and twin boundaries are coloured red.

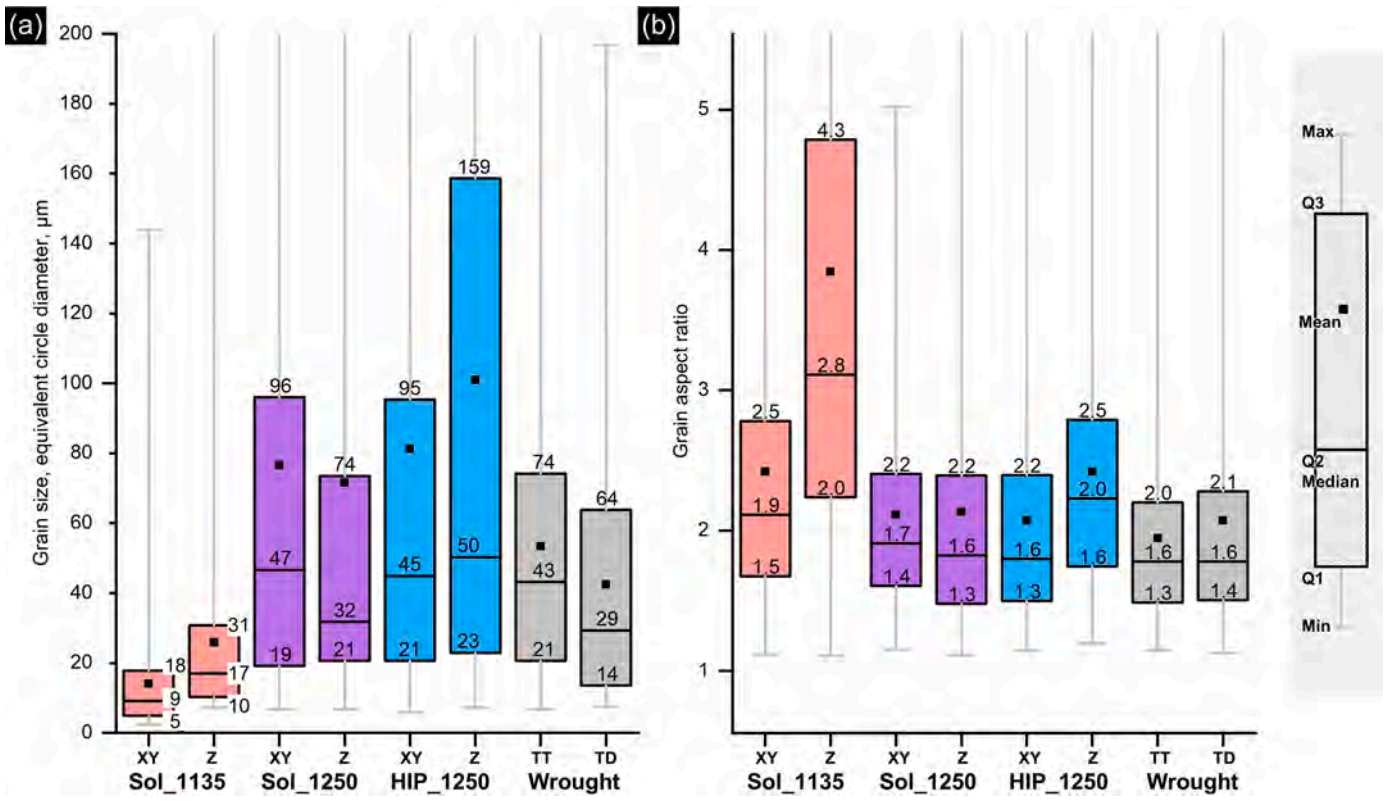

Fig. 5. Box-and-whisker plots showing (a) the distribution of grain size in equivalent circle diameter and (b) the distribution of grain aspect ratios, for different conditions in two cross-section orientations. Each plot depicts the first quartile (Q1), median (Q2), third quartile (Q3), and mean of each distribution.

Table 4
Grain boundary and twin boundary characteristics for different conditions.

Condition	Section	Total grain boundary length, µm	Twin boundary fraction	Twin boundary length, µm/µm^2	Twins per grain (average)
Sol_1135	Z	1.3E+5	–	–	–
	XY	1.8E+5	–	–	–
Sol_1250	Z	7.3E+4	0.66	4.8E+4	4.4
	XY	7.4E+4	0.69	5.1E+4	4.23
HIP_1250	Z	8.1E+4	0.65	4.6E+4	4.37
	XY	7.7E+4	0.66	5.1E+4	4.34
Wrought	TT	9.1E+4	0.62	5.6E+4	1.17
	TD	9.5E+4	0.56	5.3E+4	0.86

preferred orientation along ⟨100⟩ directions, as shown in Fig. 6(a). Contrary to this highly textured microstructure, the Wrought condition, Fig. 6(d) showed no preferred orientation in its grains. The Sol_1250, Fig. 6(b), and HIP_1250, Fig. 6(c) conditions showed weaker texture than Sol_1135, but some preferred crystal orientations close to the ⟨100⟩ directions were still retained despite the occurrence of grain growth. Note that in Fig. 6 the directions showing the highest multiples of uniform density are not fully aligned with the pole of the projection, which is probably due to deviations in the sectioning and preparation during metallography and / or slight misalignment of samples in the microscope. Inverse pole figure (IPF) orientation maps of each condition can be seen in the Supplementary Material as Figure S1.

All conditions of heat treated 282 alloy showed the presence of grain boundary carbides, intragranular carbides, grain boundary γ', and intragranular γ'. Grain boundary carbides were enriched in Cr and C and are expected to be mainly $M_{23}C_6$ carbides according to the numerous

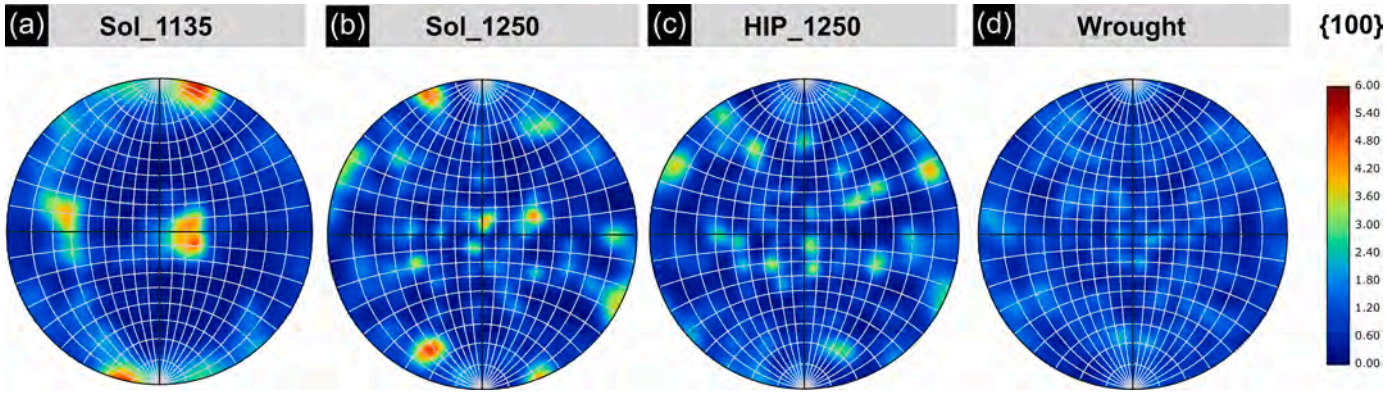

Fig. 6. (100) pole figures obtained from EBSD measurements for different conditions, (a) Sol_1135; (b) Sol_1250; (c) HIP_1250; (d) Wrought. The centre of the pole figure is oriented parallel to the building direction.

reports of the presence of that phase in heat treated 282 alloy [20–23]. The presence of $M_{23}C_6$ carbides at grain boundaries has been suggested to be essential for the creep strength and high temperature ductility of this alloy [14]. SEM-EDX analysis also showed the presence of B in certain particles at grain boundaries, which is consistent with reports in the literature of boride phases and boron-containing carbides in several alloys including 282 alloy [24,25]. M_3B_2 type borides have been predicted by CALPHAD computations by several authors [26,27] and Osoba et al. identified Mo-enriched M_5B_3 borides at grain boundaries of wrought and heat treated 282 alloy plate [28]. Mo-enriched M_6C carbides have also been widely reported in the literature for 282 alloy and are understood to be a reaction product of primary Mo,Ti-rich MC carbides, and so are not usually located at recrystallized grain boundaries [29]. The focus in the current study was placed on the major differences in distribution and morphology of grain boundary carbides between different conditions, which are understood to be more influential on mechanical performance.

The grain boundary microstructures and γ' precipitates for the Sol_1135, Sol_1250, HIP_1250, and Wrought conditions are shown in Figs. 7, 8, 9, and 10 respectively, and additional micrographs from both XY and Z cross-sections can be found in the Supplementary Material in Figures S3 to S6. The microstructure of the Sol_1135 condition was characterized by sporadically occurring grain boundary carbides and grain boundary γ', as depicted in Fig. 7. The grain boundary γ' appears lighter in contrast in the secondary electron (SE) SEM micrograph of Fig. 7(c), and the carbides appear darker in contrast. Carbides appeared globular in morphology and were widely spaced at the grain boundaries including frequently at triple points. Intragranular carbides were found to be of fine size and evenly distributed in the grain interiors, as seen in the EDX map of C in Fig. 7(c). The microstructure is in general similar to that described in a previous article by the authors [2].

In comparison to the Sol_1135 condition, grain boundaries in the Sol_1250, HIP_1250, and Wrought conditions featured fine carbides interconnected with grain boundary γ'. This structure is seen in Fig. 8(c) and Fig. 10(c) in the EDX maps. The carbides were sub-micron sized and spaced close together, forming almost continuous chains. Such carbides and γ' precipitates were also observed at twin boundaries, see Fig. 9(a). Similar observations of carbide precipitation at incoherent twin boundaries have been previously observed in wrought 282 alloy [30].

All the PBF-LB processed conditions showed fine intragranular carbides throughout the microstructure. These carbides were sub-micron sized and can be seen in Fig. 7(c) and Fig. 8(c). The Wrought condition showed coarse micron sized carbides within grains, seen in Fig. 10 (a), which appear to be located at prior interdendritic regions or prior grain boundaries [1,31–33].

The γ / γ' microstructure within grains was similar for all conditions, showing a uniform distribution of spherical precipitates, as seen in Fig. 7 (b), Fig. 8(b), Fig. 9(b), and Fig. 10(b). The intragranular γ' sizes for each condition were measured by image analysis, and the results are presented in Fig. 11. The Sol_1135 and Wrought conditions resulted in very similar γ' precipitates regarding size, having mean sizes of 50 nm and 43 nm, respectively. The Sol_1250 condition appeared to produce slightly finer γ' and the HIP_1250 condition seemed to produce slightly coarser γ' on average. The variations are likely to be due to small differences in cooling rate from the solution and first ageing treatments, which have been shown to affect γ' precipitate size [34]. However, it is notable that the standard deviations of each condition's distribution are overlapping, and the sizes are in general consistent with reported values [35–37].

3.3. Mechanical testing

A summary of the results from tensile testing at room temperature and 760 °C is shown in Fig. 12, and selected tensile curves are shown in Fig. 13. Two samples per condition were tested and the average value is presented in Fig. 12 along with error bars representing the difference between the highest / lowest value and the average. Variation in results

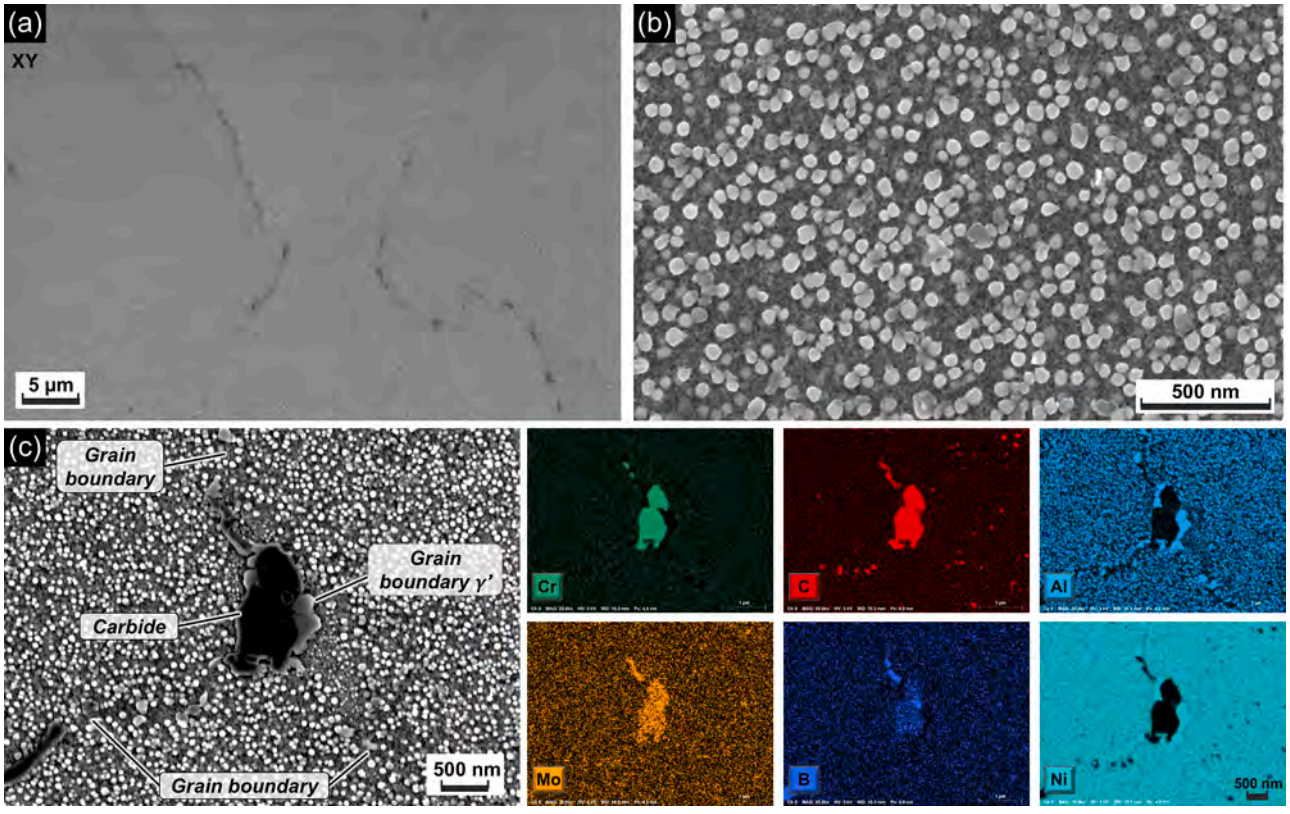

Fig. 7. SEM micrographs of the microstructure of the Sol_1135 condition: (a) microstructure overview; (b) intragranular γ' precipitates; (c) high magnification secondary electron micrograph and EDX map at grain boundary.

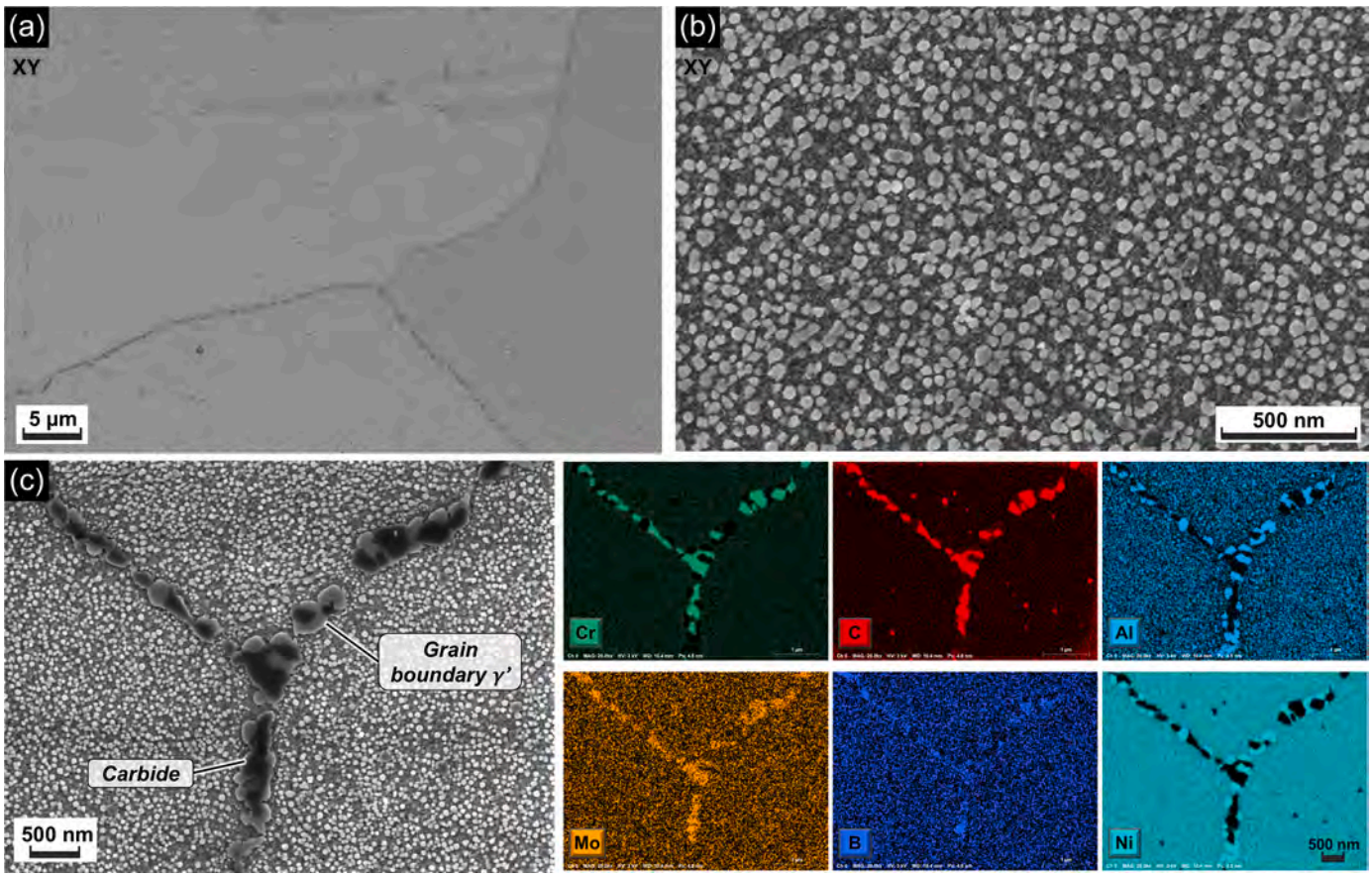

Fig. 8. SEM micrographs showing the microstructure of the Sol_1250 condition: (a) microstructure overview; (b) intragranular γ' precipitates; (c) high magnification secondary electron micrograph and EDX map at grain boundary.

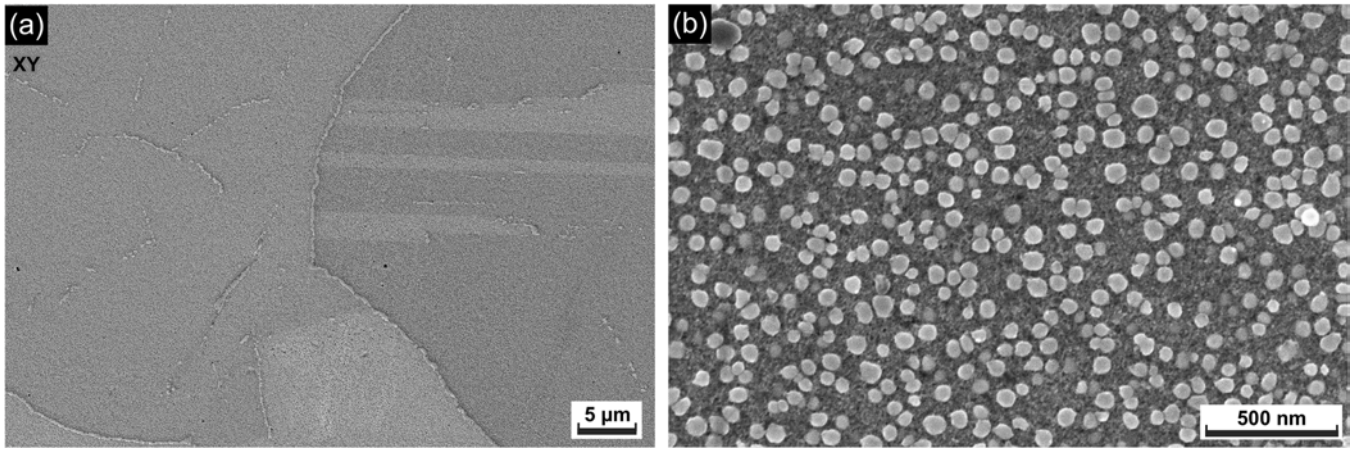

Fig. 9. SEM micrographs of the microstructure of the HIP_1250 condition: (a) microstructure overview; (b) intragranular γ' precipitates.

was small within conditions, in agreement with the microstructure observation and low fraction of defects. Only the Sol_1135 vertical orientation 760 °C tensile tests showed a deviation of more than 1 % in strength among samples, and in this case a third sample was tested to provide more representative data.

Room temperature tensile testing results showed markedly higher yield strength for the Sol_1135 condition compared to other conditions. However, Sol_1135 also showed the highest anisotropy, with vertical samples having average yield strength of 45 MPa less than horizontal. Sol_1135 samples also showed the largest difference between vertical and horizontal elongations after fracture. The Sol_1250 and HIP_1250 samples showed yield strengths roughly 200 MPa less than the Sol_1135 samples. These conditions also showed reduced difference between horizontal and vertical samples, however the horizontal samples continued to show higher strengths and lower elongations after fracture compared to vertical. The HIP_1250 samples on average showed 1 percentage point higher elongation after fracture in each orientation compared to Sol_1250, which is not considered significant given the sample size of 2 samples per condition and known natural variation in tensile testing mesurements. Wrought samples showed yield strength and elongation values generally similar to those of Sol_1250 and HIP_1250.

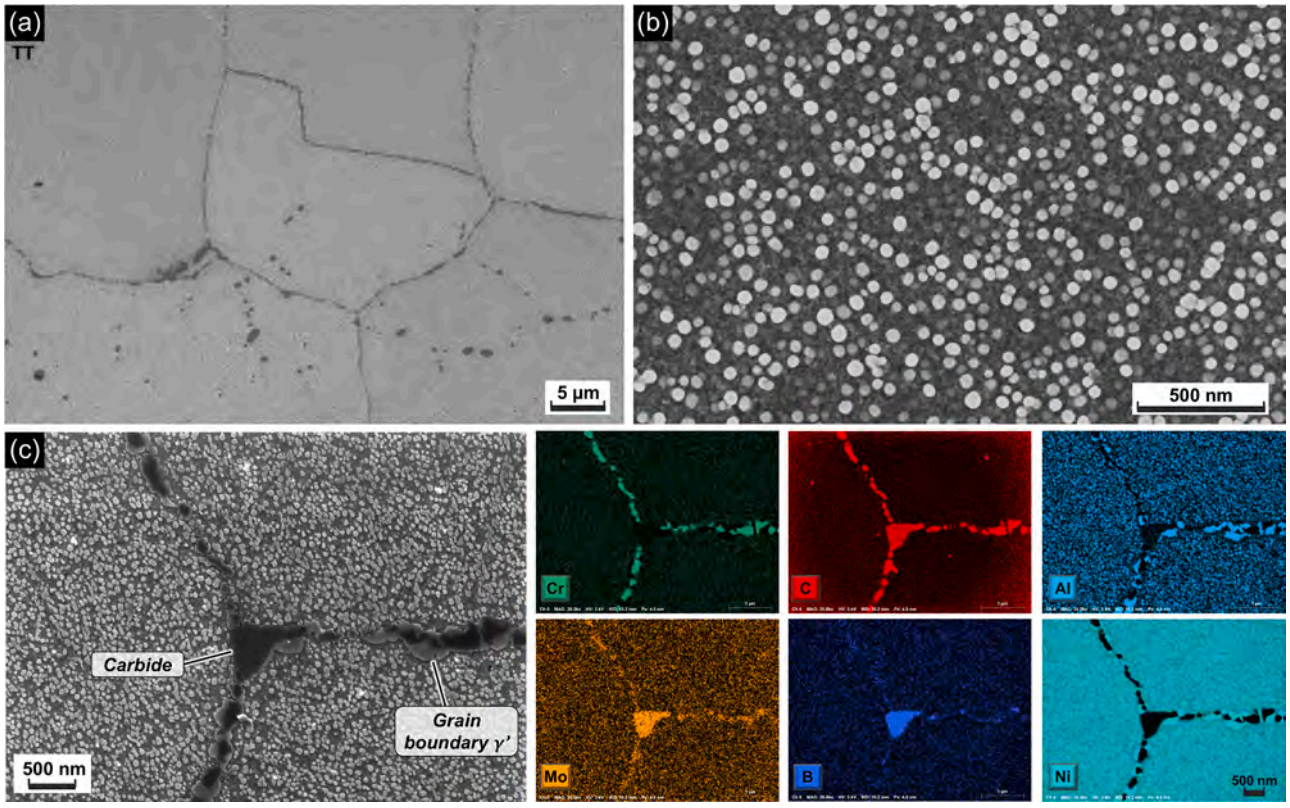

Fig. 10. SEM micrographs of the microstructure of the Wrought material: (a) microstructure overview; (b) intragranular γ' precipitates; (c) high magnification secondary electron micrograph and EDX map at grain boundary.

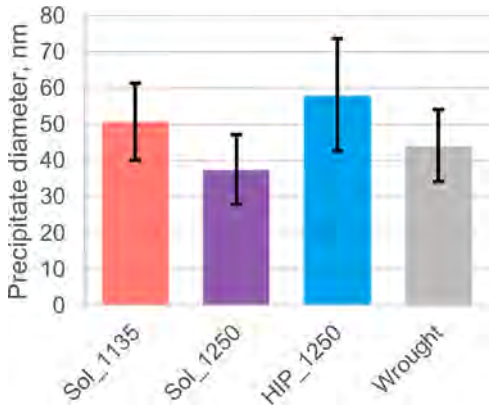

Fig. 11. Measured average size of γ' precipitates in samples of the different conditions studied. Error bars represent standard deviations.

At 760 °C the Sol_1135 condition continued to show the highest yield strengths, though a clear loss of ductility in the horizontal orientation was also observed. While vertical elongation after fracture was ~23.5 %, the horizontal elongation after fracture was only 9.0 % on average. Horizontal fracture elongation for all other conditions, however, was above 20 %. The Wrought condition and Sol_1250 produced largely similar tensile test results, as can be seen from the tensile curves in Fig. 13(b). The HIP_1250 samples showed similar yield strength as Sol_1250 and Wrought, but higher elongation after fracture and area reduction in general.

The engineering stress-strain curves also show a difference in strain hardening behaviour between the different conditions. Sol_1135 produced the least strain hardening of all tested conditions, while the strain hardening behaviour of Sol_1250 and HIP_1250 was extremely similar to that of the Wrought samples, both at room temperature and at 760 °C. Higher strain hardening ratios were observed at room temperature than at 760 °C, as depicted in Fig. 12(a) and (c). It is also notable from the stress-strain curves that the only condition to fail without prominent necking was the horizontal Sol_1135 condition at 760 °C.

Results from creep and stress rupture testing at 927 °C and 89 MPa are presented in Table 5 and creep strain curves are displayed in Fig. 14. The Wrought condition samples ruptured after 115 hrs on average with high rupture elongation of 53 % on average. Horizontal samples of the Sol_1135 condition presented the smallest rupture life and highest minimum (steady state) creep rate. Sol_1135 vertical samples showed more than double the rupture life compared to the horizontals as well as an order of magnitude lower minimum creep rate.

Notably longer rupture lives were seen in the tests of the Sol_1250 and HIP_1250 conditions, exceeding 200 hrs to rupture for most samples. Vertical samples for these conditions continued to out-perform horizontal samples, but especially notable was that horizontal samples out-performed the Wrought ones. With respect to minimum creep rate the HIP_1250 vertical sample showed the lowest rate of all tests, however in general the minimum creep rates of the Sol_1250 and HIP_1250 were consistently lower than Wrought or Sol_1135.

4. Discussion

4.1. Defects and porosity

282 alloy is generally regarded as amenable to AM, and as shown in Fig. 3 and Table 3, the PBF-LB material was generally low in porosity and defects. Boswell et al. [8] reported defect fractions between 0.05 % and 0.3 % by area which are slightly higher than observed here and in previous work [2]. Microcracking has also been reported in PBF-LB processed 282 alloy [8,38] however none was observed at any point in the current results. Although PBF-LB hardware and process

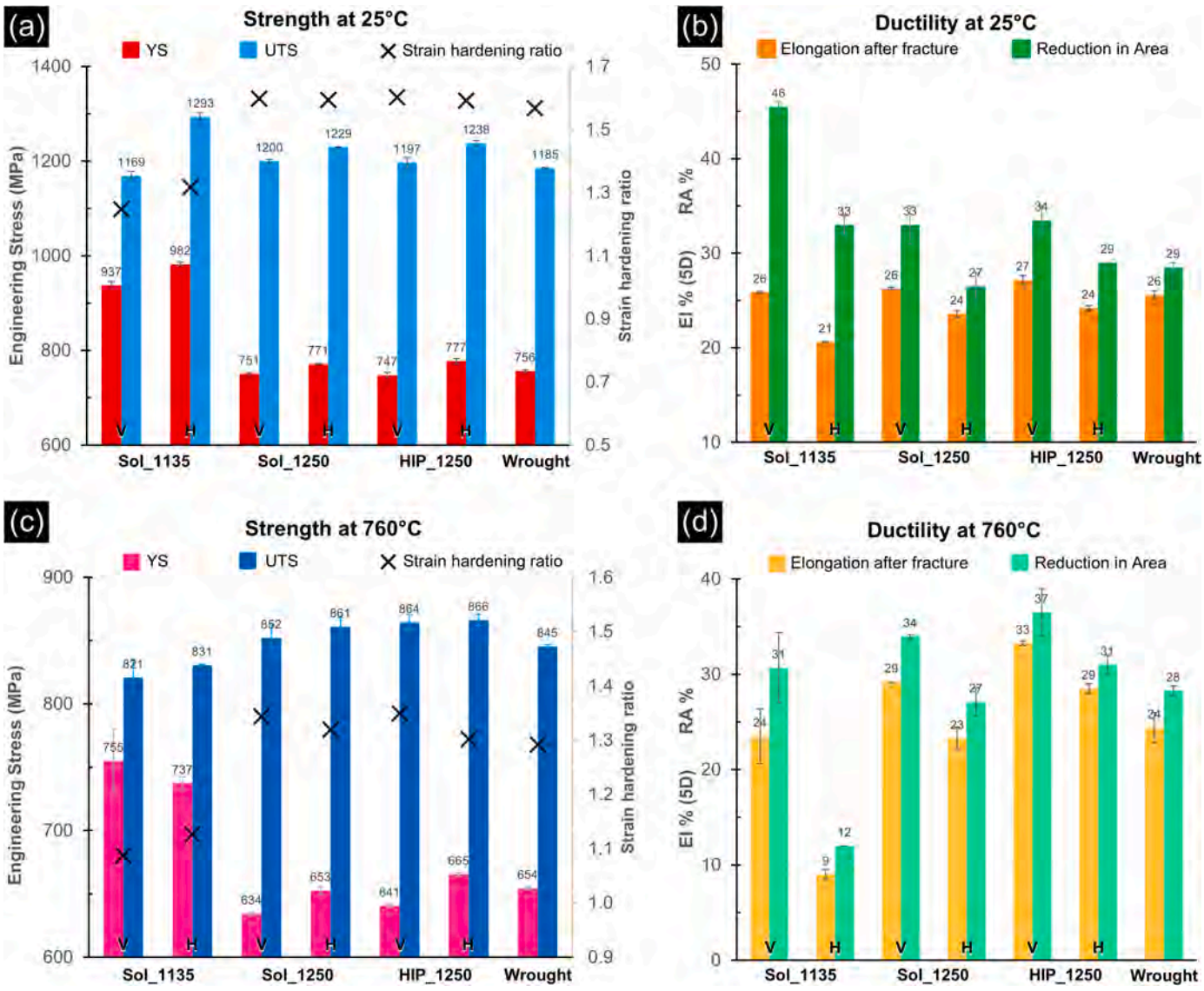

Fig. 12. Tensile testing results including yield strength, ultimate tensile strength, elongation after fracture, and reduction in area from different conditions at (a)-(b) room temperature, and (c)-(d) 760 °C.

parameters were not a variable in this study, these factors along with the powder are instrumental in producing the nearly defect-free material observed in the current results.

Post-processing by HIP at 1250 °C and 100 MPa for 4 h was successful in further reducing the porosity content of the PBF-LB processed material, as shown by the lowered defect percentage and defect counts for the HIP_1250 condition in Table 3. Note that defect analysis was done after full heat treatment, including the two-step ageing, so that any defect regrowth would be included in the porosity measurements. Benefits of the defect healing influence of HIP should be most notable in tensile elongation compared to the Sol_1250 condition, however, only a marginal improvement in tensile elongation at room temperature over the Sol_1250 condition was achieved – see Fig. 12. On the other hand, at 760 °C the HIP_1250 condition showed improvement of at least 4 percentage points of elongation after fracture over Sol_1250 in both orientations, which is significant. Since there were some minor differences between the grain sizes of Sol_1250 and HIP_1250, comparative analysis of the fracture surfaces (see Fig. 15 (c, d) and (e, f)) of the 760 °C tensile samples of Sol_1250 and HIP_1250 was performed to better understand if HIP was responsible for the increased ductility. Small pores could be observed on the Sol_1250 fracture surface, while none were found on the HIP_1250 fracture surface, suggesting that defect healing by HIP helped to delay the coalescence of voids which eventually led to fracture. While similar beneficial effects of HIP have been reported elsewhere, it is noted that the porosity content even without HIP is extremely low, and hence other factors such as grain size may also have contributory effects on ductility at 760 °C. Therefore, based on the current results, the effect of low levels of residual porosity on mechanical performance could not be determined conclusively.

Although the PBF-LB 282 alloy showed higher O and N content than wrought 282 alloy, no large oxide or nitride inclusions were observed in the material other than previously reported dispersed nano-meter scale particles [2]. Such oxides have been shown to occur in PBF-LB metals at various levels of O content [39]. The deleterious effects of nano-oxides on mechanical performance have recently been demonstrated by Peters et al. for different PBF-LB Ni-base alloys, showing that oxygen content above 0.03 wt% is particularly harmful [40]. However, this level is significantly higher than what is found in the current results.

4.2. *Heat treatment effects on grain structure and microstructure*

As shown in Figs. 4, 5, and 6, the larger grain sizes, smaller aspect

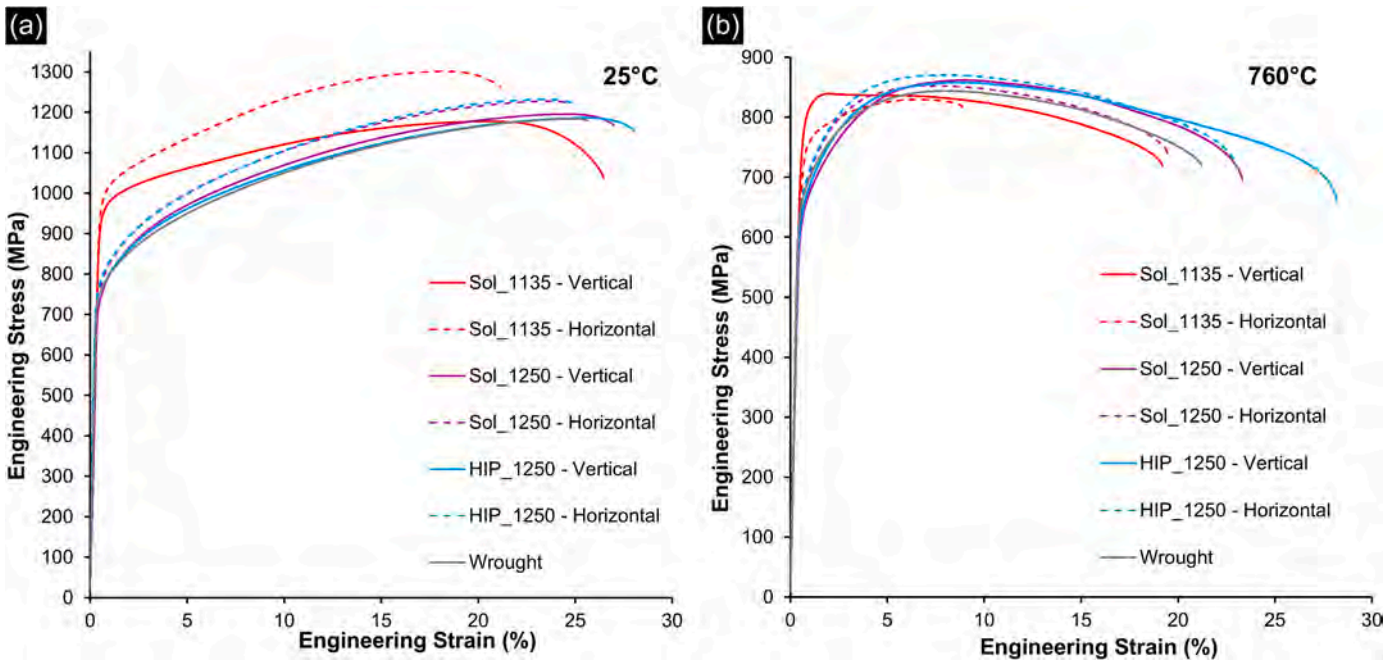

Fig. 13. Engineering stress-strain curves from tensile tests of all conditions at (a) 25 °C and (b) 760 °C.

Table 5
Creep and stress rupture testing results from all conditions.

Condition	Orientation	Temperature °C	Applied Stress, MPa	Rupture Life, hrs	Elongation after fracture %	Reduction of area %	Minimum creep rate, s^{-1}
.Sol_1135	Vertical	927	89	127.2 ± 1.2	26.0 ± 1.0	27.7 ± 0.7	3.5E-4
	Horizontal	927	89	44.1 ± 3.6	22.5 ± 1.5	26.4 ± 6.6	1.7E-3
Sol_1250	Vertical	927	89	334.2 ± 12.8	27.8 ± 0.8	20.1 ± 8.0	3.2E-5
	Horizontal	927	89	199.9 ± 27.2	11.5 ± 7.5	15.6 ± 10.5	3.0E-5
HIP_1250	Vertical	927	89	310.8 ± 35.2	20.5 ± 7.5	26.6 ± 5.5	1.7E-5
	Horizontal	927	89	247.9 ± 1.1	11.6 ± 5.5	19.2 ± 7.9	2.0E-5
Wrought	–	927	89	115.0 ± 6.0	52.6 ± 6.6	63.8 ± 3.2	1.0E-4

ratios, and weaker texture in the Sol_1250 and HIP_1250 conditions relative to Sol_1135 indicate that solution treatment at 1250 °C results in substantial changes to the grain structure, pointing to the possible activation of static recrystallization and grain growth.

The term "recrystallization“ in the context of heat treatment is most often used to refer to static primary recrystallization, wherein formation and growth of new strain-free grains occurs from a plastically deformed or dislocation-dense matrix [41]. Microstructures immediately after static recrystallization (including those of wrought 282 alloy) typically exhibit equiaxed grains and grain size finer than the microstructure prior to recrystallization [32]. Grain growth is a separate phenomenon, wherein some grains grow in size while others shrink, resulting in a larger average grain size for the microstructure. In the AM superalloy literature, however, the term “recrystallization” has mostly been used to refer to the formation of a grain structure with coarser grain size relative to as-built, and the removal of high dislocation density and cellular substructures [7,42,43], despite the understanding that grain growth is a prerequisite for a coarsened grain structure. In the following discussion the term “static recrystallization” is used to refer to recrystallization in the conventional sense, and “recrystallization” is used when referring to the common meaning taken in the AM superalloy literature.

Stored strain energy is the major driving force for static recrystallization, and the driving force for grain growth is minimization of grain boundary energy. These processes are opposed by the presence of secondary phase particles at grain boundaries, such as γ’, carbides, borides, and oxides which act to “pin" the movement of boundaries [41]. PBF-LB processed metals are known to have especially high strain energy in the as-built state [10,44], and their fine grain sizes also result in high grain boundary energy. 282 alloy in particular is amenable to static recrystallization as well as grain growth due to several factors. The carbon content is relatively low compared to most superalloys, resulting in lower efficiency of the Zener pinning effect that prevents grain boundary movement during solutionising. Boron content is also relatively low, and borides such as M_3B_2, predicted to form according to thermodynamic calculations, dissolve at ≈1195 °C [4,10]. The solvus temperature of γ’ is below 1000 °C, and the solidus temperature is rather high (≈1270 °C [7]) providing a large window for solution heat treatment. Metzler and Fahrmann showed that wrought 282 alloy after thermomechanical processing underwent recrystallization at temperatures as low as 1100 °C. Conversely, it has been reported that heat treatments in the range of 1100 °C to 1200 °C (including Sol_1135 from the current study) did not produce recrystallization in PBF-LB 282 alloy [9,10], and Christofidou et al. suggested that a minimum temperature of 1240 °C is needed to induce full recrystallization [7]. These reports from the literature and the current results suggest that relative to wrought 282 alloy, a higher temperature is needed to change the grain structure of PBF-LB 282 alloy. This may be due to the presence of nano-oxides in the microstructure, as was also suggested by Hilla et al. for PBF-LB René 65 [45]. However, pinning effects from widely distributed and stable MC carbides are expected to be a major contributing factor for this effect, as these carbides do not dissolve even up to the liquidus temperature of the alloy. The pinning effect of carbide or oxide particles may also be a factor in the tortuous grain boundary morphologies observed in the Sol_1250 and HIP_1250 conditions, which are in contrast to the relatively straight boundaries observed in the Wrought condition (see Fig. 4) [43].

Differences between the grain size and aspect ratios achieved in the

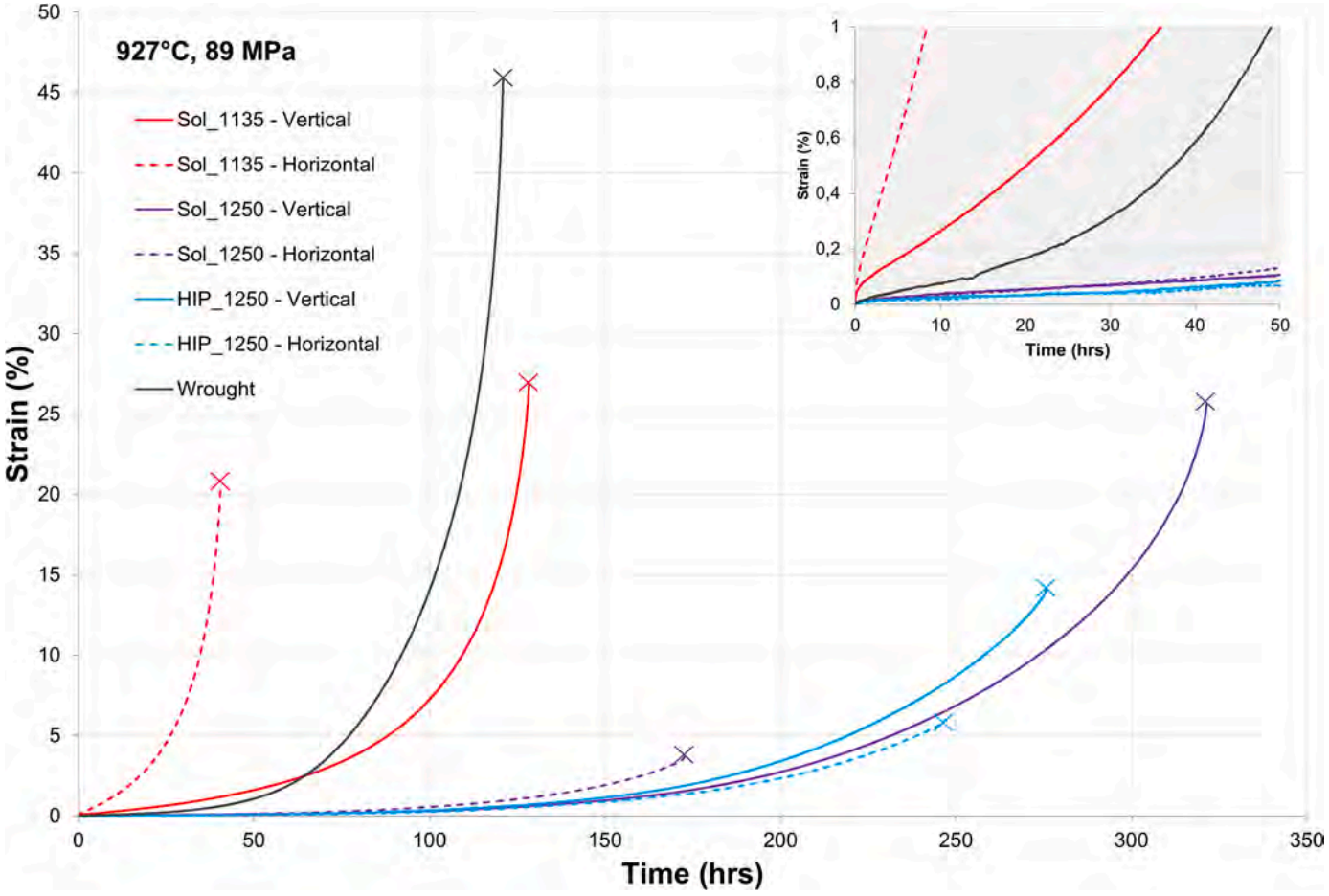

Fig. 14. Creep curves of samples of the different conditions. Inset showing the difference in minimum creep rate between different conditions.

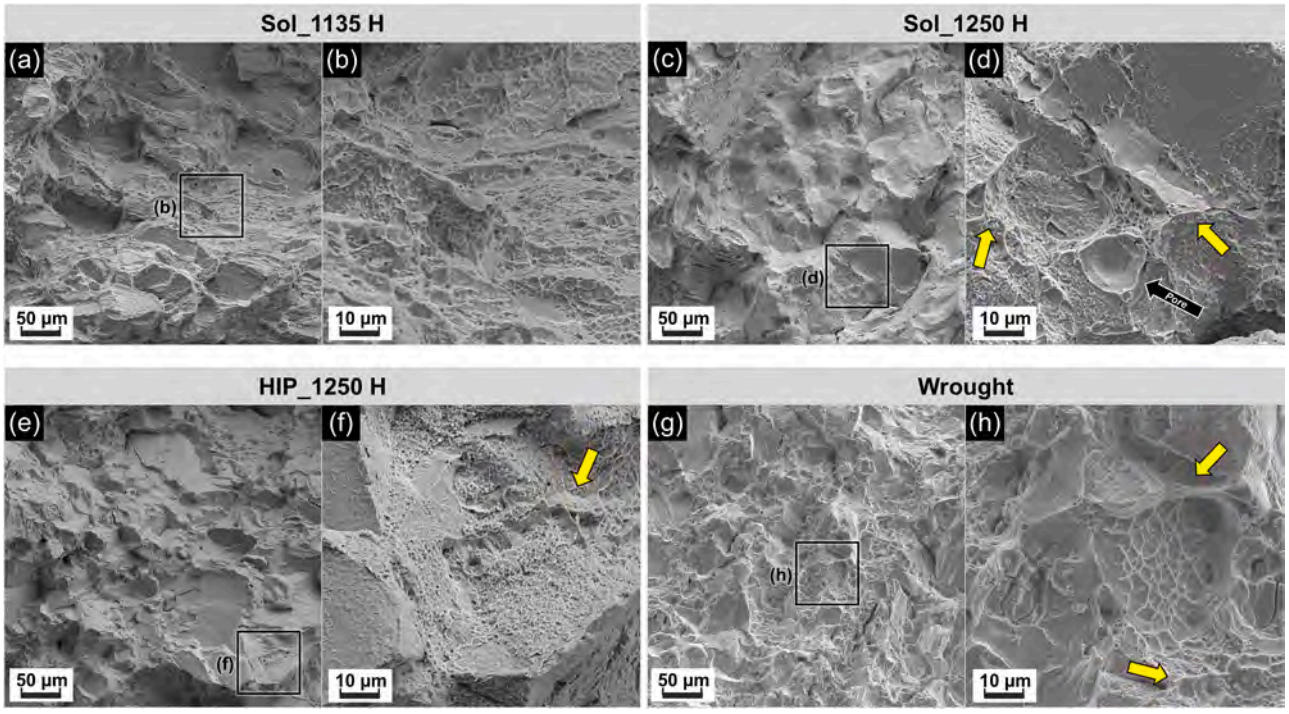

Fig. 15. Fracture surfaces from 760 °C tensile tests of the horizontal samples of (a)-(b) Sol_1135; (c)-(d) Sol_1250; (e)-(f) HIP_1250; (g)-(h) Wrought. Yellow arrows point to ductile deformation features at or near grain boundaries.

Sol_1250 and HIP_1250 conditions were mainly in the Z cross-section, where Sol_1250 appeared to produce smaller median grain size than HIP_1250. A higher frequency of very large grains was seen in the HIP_1250 condition, and the distribution showed a Q3 grain size of 159 μm ECD. The aspect ratio was also larger in the Z cross section. The longer soaking time of 4 h in HIP_1250 resulted in more pronounced grain growth, where larger grains grow at the expense of smaller grains. This is supported by the observation that Q1 grain sizes were measured to be slightly larger in both XY and Z cross-sections for HIP_1250 as compared to Sol_1250. Note that Boswell et al. performed a recrystallization heat treatment at 1250 °C for 1 hour and reported a bimodal grain size, with the largest grains up to 563 μm and smallest only 2 μm in diameter [8]. This suggests that a longer soaking time than 1 hour may have some benefit in reducing variation in grain size.

In addition to grain size which was larger than for the Wrought condition, the Sol_1250 and HIP_1250 microstructures were distinguished by a higher twin boundary fraction and widespread distribution of small twins. The presence of twins in wrought 282 alloy, as well as recrystallized PBF-LB 282 alloy has been commonly reported [7,18,24]. According to the most commonly applied growth accident model of twin formation, a low stacking fault energy, a small starting grain size, and a high grain boundary velocity favour the frequent formation of twins. The stacking fault energy for 282 alloy is estimated to be quite low at 27.63 mJ/m^2 [46], fine grain size in as-built condition has also been observed [2,37], and these factors coupled with high strain energy and hence high grain boundary velocity in as-built condition may explain the observed higher frequency of twin boundary formation.

The above results and discussion clearly demonstrate that heat treatment at 1250 °C results in grain growth in PBF-LB 282 alloy. However, it is not clear whether this grain growth is preceded by static recrystallization, or if the reduction in dislocation density has primarily occurred through static recovery. Upon occurrence of static recrystallization, grains are equiaxed and grain size is small, but is subsequently enlarged during grain growth. Typically, wrought Ni-base alloys that undergo static recrystallization followed by grain growth exhibit equiaxed grains of uniform grain size, with smooth grain boundaries, and without pronounced texture, such as the Wrought condition shown previously, or as depicted in the literature [17,32]. Conversely, if static recrystallization does not occur, grains grow starting from their original size, and retaining their original orientation, similar to the Sol_1250 and HIP_1250 conditions. Therefore, the observations of large spread in grain size, irregular grain morphology, large aspect ratio grains in the building direction, and residual texture in the Sol_1250 and HIP_1250 conditions appear to indicate that static recrystallization did not precede grain growth. Further heat treatment tests are necessary to study the kinetics of the grain structure transformation, which should help to establish the occurrence or absence of static recrystallization.

The change in grain boundary carbide frequency from sporadic in Sol_1135 to closely spaced in Sol_1250, HIP_1250, and Wrought conditions is understood to be a consequence of the change in grain size. Carbides form preferentially at grain boundaries because solubility of C in the γ matrix is much lower than the amount of C present in the alloy. The amount of C available to form the carbides is equal in all conditions, but grain boundary area (or volume) is much smaller in the microstructures where grain size is larger, i.e. Sol_1250, HIP_1250, and Wrought conditions. This results in carbides (and grain boundary γ') forming with close spacing during the first ageing heat treatment step at 1010 °C [36].

4.3. Comparative mechanical performance

The layer-wise nature of the PBF-LB process results in direction dependent mechanical properties, as shown in current and previous results [2]. In particular, horizontal tensile elongation after fracture at 760 °C was only 9 % for the Sol_1135 condition compared to 24 % for the Wrought condition. Ductility in the horizontal (as well as vertical) orientation was improved in Sol_1250 and HIP_1250 conditions to the same level as the Wrought condition or even higher. Fractographic study of the horizontally oriented 760 °C tensile specimens was performed to better understand the cause of this improvement, and prominent features of the fracture surfaces are shown in Fig. 15. The figure shows that fracture was primarily intergranular in all four conditions, however the Sol_1250, HIP_1250, and Wrought conditions showed ductile tearing evidenced by fine dimples at grain boundaries where carbides would be present. A similar observation was also made by Joseph et al. in wrought 282 alloy [36]. The literature on polycrystalline superalloy strengthening mechanisms also suggests that when carbides are formed at grain boundaries, they are usually surrounded by a softer and more ductile region either due to the formation of grain boundary γ' [33] or by depletion of solid solution strengthening elements from the matrix [47]. It is therefore understandable that a more frequent occurrence of carbides and grain boundary γ' as seen in the Sol_1250, HIP_1250, and Wrought conditions would produce the ductile fracture effects seen on grain boundaries at fracture surfaces and thence the improvement in ductility. The lowered horizontal tensile ductility in the Sol_1135 condition may also be related to the highly textured grain structure in that condition, leading to differences in Taylor factor with loading direction, as shown by Deng et al. for PBF-LB IN718 [48]. Yu et al. also attributed strongly anisotropic high temperature ductility in PBF-LB Hastelloy X to the highly textured grain structure [44].

Another noticeable difference in tensile performance when comparing Sol_1135 to the Sol_1250 and HIP_1250 conditions was the reduction in yield strength at room temperature and 760 °C, which is explained by the grain size strengthening effect. Fine grain size in Sol_1135 results in higher strength according to the well-known Hall-Petch relation, and this level of strengthening contribution is no longer active when the grain size is increased in the Sol_1250 and HIP_1250 conditions. Santella et al. observed the same effect when conducting comparative tensile tests of wrought 282 alloy with different grain sizes at 760 °C [17]. Note that the rule of thumb stating that grain size strengthening ceases to be effective above $\approx 0.5T_m$ [33] seems not to apply in this alloy, as 760 °C is equal to $0.6T_m$ for 282 alloy.

The most prominent improvement in properties from the Sol_1250 and HIP_1250 heat treatments were in creep rupture life and minimum creep rate. The rupture lives resulting from these conditions were at least 100 h longer than in the corresponding orientation for the Sol_1135 condition. The greatest improvement was seen in the horizontally oriented specimens. Minimum creep rates were an order of magnitude lower and onset of tertiary creep was also delayed in the Sol_1250 and HIP_1250 specimens compared to Sol_1135 and Wrought conditions.

The ruptured creep test samples were analysed as shown in Fig. 16. Cross-sections of ruptured bars for the Wrought condition, as well as Sol_1250, HIP_1250, and vertical Sol_1135 conditions, showed formation of voids at grain boundaries perpendicular to the stress axis, which were in tension during testing (see Fig. 16(b) to (g)). This suggests that the test condition of 927 °C and 89 MPa resulted in occurrence of diffusional flow either at grain boundaries or within the grain bulk, leading to cavitation, grain boundary sliding, and eventual fracture of the specimen. Conversely, cross-sections of the ruptured Sol_1135 horizontal bars (see Fig. 16(a)) showed intragranular cracks along columnar grains perpendicular to the axis of applied stress, with no wide cavities forming such as those seen in Wrought or other conditions. Grain boundaries are known to be fast paths for diffusion, and as shown in Table 4, Sol_1135 has the largest amount of grain boundaries of all the conditions. This suggests that diffusional flow occurred faster in the Sol_1135 condition, but the columnar morphology and highly textured grain structure could not accommodate sliding, resulting in intergranular detachment. The flat fracture surface also suggests that the orientation of the grains relative to the stress axis provided multiple sites for fracture to initiate and rapidly propagate, which explains the short time to rupture. Conversely, in the Sol_1135 vertical specimens, sliding of grain boundaries to accommodate cavitation could take place due to the

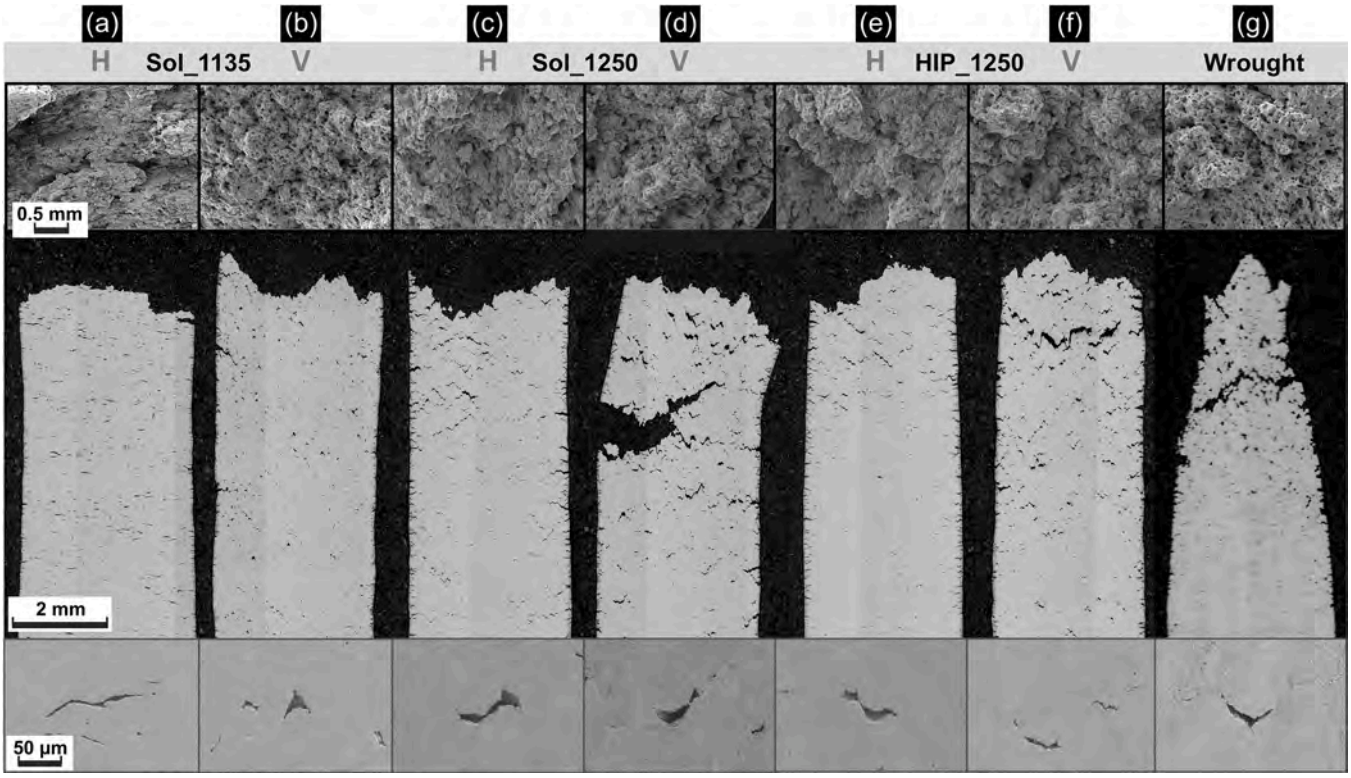

Fig. 16. Fracture surface and cross-sections of creep tested specimens of (a)-(b) Sol_1135; (c)-(d) Sol_1250; (e)-(f) HIP_1250; (g) Wrought.

orientation of the columnar structure along the axis of applied stress. Creep rate was also lower as the majority of grain boundaries were parallel to the stress axis.

Crept specimens from the Sol_1250 and HIP_1250 conditions showed cavitation very similar to that observed in specimens from the Wrought condition as seen in Figs. 16(c) to (g). One factor which may explain the increase in rupture lives for these conditions is the increased grain size [49], as previously discussed. This is directly related to retardation of creep processes, especially at high temperature and low stress conditions, as shown by Santella et al. for wrought 282 alloy [17]. The random texture, relative to Sol_1135, may also be a factor in better creep performance, as suggested by Prasad et al. [50]. The microstructure consisting of closely spaced grain boundary carbides and grain boundary γ' is also expected to be an important contributor to the improved creep performance. According to the literature these carbides act to pin grain boundaries and retard sliding, while the ductile grain boundary γ' prevents cracking of the brittle carbides [33]. Intragranular carbides, however, may also play a role in the improved creep performance of Sol_1250 and HIP_1250 over Wrought. According to the model by Lapera et al., these carbides slow down the supply of dislocations travelling from the grain interior to the grain boundary, thereby inhibiting creep by sliding of grain boundaries [51]. As seen by comparing Figs. 8, 9, and 10, the Sol_1250 and HIP_1250 conditions appear to have finer and more widely dispersed intragranular carbides compared to Wrought.

A further factor which suggests Sol_1250 and HIP_1250 having more creep resistant microstructure than Wrought is the occurrence of tortuous grain boundaries, seen in Fig. 4, which inhibit sliding owing to their geometry. The Wrought condition by comparison has very straight grain boundaries. The increased frequency of twin boundaries may also contribute to the longer rupture life and lower creep rate, as shown by several studies on grain boundary engineering of superalloys where creep rates were lowered by increased twin boundary fractions. Twin boundaries and other coincidence site lattice (CSL) boundaries are known to be low energy boundaries due to their ordered orientation and have been shown to retard creep by trapping dislocations and creating back-stresses on the following dislocations, thereby reducing the effective stress [52,53]. A non-linear model for the creep rate dependence on fraction on CSL boundaries was proposed [52], which suggests that even a small increase in CSL boundary percentage, as seen in Table 4, can result in a significant reduction in creep rate. Further investigation is required to pinpoint the most critical factors for the improved creep performance of the Sol_1250 and HIP_1250 conditions.

4.4. Points for adoption and further research

The results in the current work clearly show that the application of a 1250 °C solution heat treatment can eliminate anisotropy of mechanical properties of PBF-LB processed 282 alloy. The creep performance in the horizontal orientation can also be improved to meet the requirements of aerospace material standards for wrought 282 alloy. However, it was noted in tensile testing and creep testing results that while Sol_1250 and HIP_1250 showed more isotropic properties relative to Sol_1135, there was still some residual anisotropy, i.e. horizontal specimens continued to show marginally higher strength, lower ductility, and shorter creep life than vertical ones. While this may be correlated with the residual texture [54], no clear explanation is currently offered and similar tests by Boswell et al. [8] also found from statistical analysis of stress rupture data that vertical specimens exhibited longer rupture life. It may also be prudent to consider that the current testing regime of high temperature and low stress probably favours diffusional creep mechanisms over power law creep, and different creep conditions, e.g. lower temperature and high stress, may not necessarily result in such competitive creep performance relative to wrought as seen here [17].

The low spread in data for tensile and creep testing suggests that the Sol_1250 and HIP_1250 heat treatments are fairly robust. The improved rupture life and lower creep rate resulting from the Sol_1250 and HIP_1250 may allow longer lifetimes or harsher service conditions for PBF-LB 282 alloy components than previously considered possible. However, heat treatments at such high temperatures are not always

practical due to heat treatment hardware limitations, and also due to distortion of complex shaped or thin-walled AM components which may occur owing to very low strength at high temperatures such as 1250 °C. The Sol_1135 heat treatment may in such cases be a good alternative, as well as in cases where designs are strength limited rather than creep limited.

5. Conclusions

An evaluation of different solution heat treatments for PBF-LB 282 alloy was performed and benchmarked to wrought 282 alloy. Testing included orientations parallel to the building direction (vertical) and perpendicular to the building direction (horizontal). The results showed that when the typical solution treatment at 1135 °C (Sol_1135) for 282 alloy was applied to PBF-LB processed 282 alloy, a highly textured and fine columnar grained microstructure was formed, which produced very high room temperature yield strength of ~980 MPa (horizontal) and ~940 MPa (vertical) compared to ~755 MPa for the Wrought material. However, the high temperature performance, particularly ductility and creep rupture performance in the horizontal orientation, was inferior relative to wrought 282 alloy.

A heat treatment at 1250 °C (Sol_1250) allowed to increase the room temperature ductility of PBF-LB 282 alloy to levels of 24–26 %, largely in line with wrought material (25.6 %). The typical anisotropy often encountered in PBF-LB alloys was also reduced, and elongations after fracture exceeding 20 % could be achieved in both tested orientations at 760 °C. Most notably, the Sol_1250 heat treatment improved the creep rupture life of PBF-LB 282 alloy at 927 °C and 89 MPa by about 2 to 5 times (between 200 and 335 h) compared to the Sol_1135 heat treatment (44 h for horizontal and 127 h for vertical orientation) and almost three time higher than for wrought material (115 h). Hence, when compared to wrought 282 alloy, the rupture life was improved by ≈100 h and minimum creep rate was reduced by an order of magnitude, which has not been reported before. Coarser grain size, tortuous grain boundaries, increased twin boundary fraction, and grain boundary microstructure (consisting of fine interconnected carbides and grain boundary γ') closely resembling wrought were identified as probable contributory factors for the improvement.

A further advantage in high temperature ductility could be gained with the application of HIP within the 1250 °C heat treatment. The results emphasize the readiness of 282 alloy as an alloy primed for adoption in AM applications and further highlight the importance of tailored heat treatments for additive manufactured superalloys.

Data availability

The raw/processed data required to reproduce these findings cannot be shared at this time due to legal or ethical reasons.

CRediT authorship contribution statement

Abdul Shaafi Shaikh: Writing – original draft, Visualization, Validation, Methodology, Investigation, Formal analysis, Data curation, Conceptualization. **Emil Eriksson:** Writing – review & editing, Investigation, Formal analysis. **Magnus Hörnqvist Colliander:** Writing – review & editing, Validation, Supervision, Methodology, Conceptualization. **Kevin Minet-Lallemand:** Supervision, Funding acquisition, Conceptualization. **Eduard Hryha:** Writing – review & editing, Validation, Supervision, Resources, Project administration, Funding acquisition, Conceptualization.

Declaration of competing interest

The authors declare that they have no known competing financial interests or personal relationships that could have appeared to influence the work reported in this paper.

Acknowledgement

This work has been performed in the framework of the Centre for Additive Manufacturing – Metal (CAM^2), financed by Vinnova. The authors gratefully acknowledge supply of wrought material from Haynes International. Johannes Gårdstam and James Shipley of Quintus Technologies are gratefully acknowledged for performing the HIP treatment.

Note: "Haynes" and "282″ are registered trademarks of Haynes international, Inc., Kokomo, Indiana, USA.

Supplementary materials

Supplementary material associated with this article can be found, in the online version, at doi:10.1016/j.mtla.2025.102334.

References

[1] K.L. Kruger, Haynes 282 Alloy. Materials For Ultra-Supercritical and Advanced Ultra-Supercritical Power Plants, Elsevier, 2017, pp. 511–545.
[2] A.S. Shaikh, F. Schulz, K. Minet-Lallemand, E. Hryha, Microstructure and mechanical properties of Haynes 282 superalloy produced by laser powder bed fusion, Mater. Today Commun. 26 (2021) 102038, https://doi.org/10.1016/j.mtcomm.2021.102038.
[3] K.A. Unocic, M.M. Kirka, E. Cakmak, D. Greeley, A.O. Okello, S. Dryepondt, Evaluation of additive electron beam melting of Haynes 282 alloy, Materials Science and Engineering: A (2019) 138607, https://doi.org/10.1016/j.msea.2019.138607.
[4] A. Ramakrishnan, G.P. Dinda, Microstructure and mechanical properties of direct laser metal deposited Haynes 282 superalloy, Materials Science and Engineering: A 748 (2019) 347–356, https://doi.org/10.1016/j.msea.2019.01.101.
[5] L. Rickenbacher, T. Etter, S. Hövel, K. Wegener, High temperature material properties of IN738LC processed by selective laser melting (SLM) technology, Rapid Prototyp. J. 19 (2013) 282–290.
[6] K. Kunze, T. Etter, J. Grässlin, V. Shklover, Texture, anisotropy in microstructure and mechanical properties of IN738LC alloy processed by selective laser melting (SLM), Mater. Sci. Eng. A. 620 (2015) 213–222, https://doi.org/10.1016/j.msea.2014.10.003.
[7] K.A. Christofidou, H.T. Pang, W. Li, Y. Pardhi, C.N. Jones, N.G. Jones, H.J. Stone, Microstructural Control and Optimization of Haynes 282 Manufactured Through Laser Powder Bed Fusion, in: S. Tin, M. Hardy, J. Clews, J. Cormier, Q. Feng, J. Marcin, C. O'Brien, A. Suzuki (Eds.), Superalloys 2020, Springer International Publishing, Cham, 2020, pp. 1014–1023.
[8] J. Boswell, J. Jones, N. Barnard, D. Clark, M. Whittaker, R. Lancaster, The effects of energy density and heat treatment on the microstructure and mechanical properties of laser additive manufactured Haynes 282, Mater. Des. 205 (2021) 109725, https://doi.org/10.1016/j.matdes.2021.109725.
[9] N. Ahmad, R. Ghiaasiaan, P.R. Gradl, S. Shao, N. Shamsaei, Low cycle fatigue behavior of additively manufactured Haynes 282: Effect of post-processing and test temperature, Int. J. Fatigue 176 (2023) 107880, https://doi.org/10.1016/j.ijfatigue.2023.107880.
[10] J. Gonzalez, Y. Zhang, A. Wessman, J. Klemm-Toole, Understanding Annealing Behavior During Post-Built Heat Treatment of Ni-Based Alloys Across Additive Manufacturing Processes, in: E.A. Ott, J. Andersson, C. Sudbrack, Z. Bi, K. Bockenstedt, I. Dempster, M. Fahrmann, P. Jablonski, M. Kirka, X. Liu, D. Nagahama, T. Smith, M. Stockinger, A. Wessman (Eds.), Proceedings of the 10th International Symposium on Superalloy 718 and Derivatives, Springer Nature Switzerland, Cham, 2023, pp. 613–627.
[11] A. Deshpande, S.Deb Nath, S. Atre, K. Hsu, Effect of Post Processing Heat Treatment Routes on Microstructure and Mechanical Property Evolution of Haynes 282 Ni-Based Superalloy Fabricated with Selective Laser Melting (SLM), Metals. (Basel) 10 (2020) 629, https://doi.org/10.3390/met10050629.
[12] AMS5951A For Haynes 282: Nickel Alloy, Corrosion and Heat-Resistant, Sheet, Strip, and Plate 57Ni - 20Cr - 10Co - 8.5Mo - 2.1Ti - 1.5Al - 0.005B Vacuum Induction and Consumable Electrode Melted, Solution Heat Treated Precipitation Heat Treatable, SAE InternationalSAE International, Amsterdam, Netherlands, 2010.
[13] Haynes International Inc., HAYNES® 282®Alloy, https://haynesintl.com/alloys/alloy-portfolio_/High-temperature-Alloys/HAYNES282alloy.aspx.
[14] L.M. Pike, Development of a Fabricable Gamma Prime Strengthened Superalloy, in: Roger C. Reed, Kenneth A. Green, Pierre Caron, Tim Gabb, Michael G. Fahrmann, Eric S. Huron, Shiela A. Woodard (Eds.), Superalloys 2008 (11th International Symposium), TMS, pp. 191–200.
[15] B. Beausir, J.J. Fundenberger, ATEX: Analysis Tools For Electron and X-ray Diffraction, ATEX, Université de Lorraine, Metz, 2017.
[16] J.N. DuPont, S.D. Kiser, J.C. Lippold, Welding Metallurgy and Weldability of Nickel-base Alloys, John Wiley & Sons, Hoboken, New Jersey, 2009.
[17] M.L. Santella, P.F. Tortorelli, M. Render, B. Pint, H. Wang, V. Cedro, X. Chen, Effects of applied stress and grain size on creep-rupture lifetime prediction for Haynes 282 alloy, Materials Science and Engineering: A 838 (2022) 142785, https://doi.org/10.1016/j.msea.2022.142785.

[18] C.J. Boehlert, S.C. Longanbach, A comparison of the microstructure and creep behavior of cold rolled HAYNES® 230 alloy™ and HAYNES® 282 alloy™, Materials Science and Engineering: A 528 (2011) 4888–4898, https://doi.org/10.1016/j.msea.2011.03.019.

[19] Ceena Joseph, Magnus Hörnqvist, Rebecka Brommesson, Christer Persson, Influence of carbide distribution on ductility of Haynes 282 forgings, in: M. C. Hardy (Ed.), Superalloys 2016: Proceedings of the 13th International Symposium on Superalloys; sponsored by the Seven Springs International Symposium Committee in cooperation with the High Temperature Alloys Committee of the Structural Materials Division of TMS (The Minerals, Metals & Materials Society) and co-sponsored by ASM International and IOM³ (The Institute of Materials, Minerals and Mining); held September 11-15, 2016 at the Seven Springs Mountain Resort, Seven Springs, Pennsylvania, USA, Wiley, Hoboken, New Jersey, 2016.

[20] C. Joseph, C. Persson, M.Hörnqvist Colliander, Precipitation Kinetics and Morphology of Grain Boundary Carbides in Ni-Base Superalloy Haynes 282, Metall Mater Trans A 51 (2020) 6136–6141, https://doi.org/10.1007/s11661-020-06019-1.

[21] L.O. Osoba, R.G. Ding, O.A. Ojo, Improved Resistance to Laser Weld Heat-Affected Zone Microfissuring in a Newly Developed Superalloy HAYNES 282, Metall and Mat Trans A 43 (2012) 4281–4295, https://doi.org/10.1007/s11661-012-1212-7.

[22] F. Hanning, A.K. Khan, J. Steffenburg-Nordenström, O. Ojo, J. Andersson, Investigation of the Effect of Short Exposure in the Temperature Range of 750–950°C on the Ductility of Haynes® 282® by Advanced Microstructural Characterization, Metals. (Basel) 9 (2019) 1357, https://doi.org/10.3390/met9121357.

[23] H. Zhang, Y. Wang, R.R. de Vecchis, W. Xiong, Evolution of carbide precipitates in Haynes® 282 superalloy processed by wire arc additive manufacturing, J. Mater. Process. Technol. 305 (2022) 117597, https://doi.org/10.1016/j.jmatprotec.2022.117597.

[24] M.G. Fahrmann, L.M. Pike, Experimental TTT Diagram of HAYNES 282 Alloy, in: E. Ott, X. Liu, J. Andersson, Z. Bi, K. Bockenstedt, I. Dempster, J. Groh, K. Heck, P. Jablonski, M. Kaplan, D Nagahama, C. Sudbrack (Eds.), Proceedings of the 9th International Symposium on Superalloy 718 & Derivatives: Energy, Aerospace, and Industrial Applications, Springer International Publishing, Cham, 2018, pp. 565–578.

[25] K.M. Delargy, G.D. Smith, Phase Composition and Phase Stability of a HIgh-Chromium Nickel-Based Superalloy IN939, Metall. Trans. A 14A (1983) 1771–1783.

[26] S. Mukherjee, S. Sivaprasad, S. Tarafder, D. Bhattacharyya, S.K. Kar, Influence of ageing on high temperature tensile deformation of a Ni-based superalloy, HAYNES 282, J. Alloys. Compd. 917 (2022) 165430, https://doi.org/10.1016/j.jallcom.2022.165430.

[27] Y. Yang, Microstructural Evolution in Cast Haynes 282 for Application in Advanced Powerplants, in: D. Gandy, J. Shingledecker (Eds.), Advances in Materials Technology for Fossil Power Plants: Proceedings from the Seventh International Conference (EPRI 2013), Waikoloa, Hawai, ASM International, 2013, pp. 143–154.

[28] L.O. Osoba, A.K. Khan, O.A. Ojo, Identification of Mo-based Precipitates in Haynes 282 Superalloy, Metall and Mat Trans A 48 (2017) 1540–1543, https://doi.org/10.1007/s11661-017-3999-8.

[29] A. Polkowska, W. Polkowski, M. Warmuzek, N. Cieśla, G. Włoch, D. Zasada, R. M. Purgert, Microstructure and Hardness Evolution in Haynes 282 Nickel-Based Superalloy During Multi-variant Aging Heat Treatment, J. of Materi Eng and Perform 28 (2019) 3844–3851, https://doi.org/10.1007/s11665-019-3886-0.

[30] E. Eriksson, J. Andersson, M.Hörnqvist Colliander, The Effect of Grain Boundary Carbides on Dynamic Recrystallization During Hot Compression of Ni-Based Superalloy Haynes 282, Metall Mater Trans A 53 (2022) 29–38, https://doi.org/10.1007/s11661-021-06524-x.

[31] M.C. Hardy, M. Detrois, E.T. McDevitt, C. Argyrakis, V. Saraf, P.D. Jablonski, J. A. Hawk, R.C. Buckingham, H.S. Kitaguchi, S. Tin, Solving Recent Challenges for Wrought Ni-Base Superalloys, Metall and Mat Trans A 51 (2020) 2626–2650, https://doi.org/10.1007/s11661-020-05773-6.

[32] D. Metzler, M.G. Fahrmann, The Effect of Prior TMP on Annealed Grain Size in HAYNES 282 Alloy, in: E. Ott, A. Banik, J. Andersson, I. Dempster, T. Gabb, J. Groh, K. Heck, R. Helmink, X. Liu, A. Wusatowska-Sarnek (Eds.), 8th International Symposium on Superalloy 718 and Derivatives, Hoboken, NJ, USA, John Wiley & Sons, Inc, 2014, pp. 379–389.

[33] C.T. Sims, N.S. Stoloff, W.C. Hagel, Superalloys II: High-Temperature Materials For Aerospace and Industrial Power, Wiley, New York, USA, 1987.

[34] C. Joseph, M. Thuvander, C. Persson, M. Hörnqvist Colliander, Precipitation of γ' during cooling of nickel-base superalloy Haynes 282, Philos. Mag. Lett. 101 (2021) 30–39, https://doi.org/10.1080/09500839.2020.1841314.

[35] P. Zhang, Y. Yuan, H. Yin, Y. Gu, J. Wang, M. Yang, G. Yang, X. Song, Tensile Properties and Deformation Mechanisms of Haynes 282 at Various Temperatures, Metall and Mat Trans A 49 (2018) 1571–1578, https://doi.org/10.1007/s11661-018-4515-5.

[36] C. Joseph, C. Persson, M.Hörnqvist Colliander, Influence of heat treatment on the microstructure and tensile properties of Ni-base superalloy Haynes 282, Materials Science and Engineering: A 679 (2017) 520–530, https://doi.org/10.1016/j.msea.2016.10.048.

[37] R. Ghiaasiaan, N. Ahmad, P.R. Gradl, S. Shao, N. Shamsaei, Additively manufactured Haynes 282: effect of unimodal vs. bimodal γ'- microstructure on mechanical properties, Materials Science and Engineering: A 831 (2022) 142234, https://doi.org/10.1016/j.msea.2021.142234.

[38] R. Otto, V. Brøtan, A.S. Azar, O. Åsebø, Processing of Haynes® 282® Alloy by Laser Powder Bed Fusion Technology, in: TMS 2019 148th Annual Meeting & Exhibition Supplemental Proceedings, Springer International Publishing, Cham, 2019, pp. 503–510.

[39] D. Riabov, M. Rashidi, E. Hryha, S. Bengtsson, Effect of the powder feedstock on the oxide dispersion strengthening of 316L stainless steel produced by laser powder bed fusion, Mater. Charact. 169 (2020) 110582, https://doi.org/10.1016/j.matchar.2020.110582.

[40] M. Peters, E.G. Brodie, S. Thomas, L. Djumas, M. Brameld, M. Salasi, Z. Quadir, M. Iannuzzi, J. Wang, T. Sercombe, C. Hutchinson, On the importance of nano-oxide control in laser powder bed fusion manufactured Ni-based alloys to enhance fracture properties, Materialia (Oxf) 32 (2023) 101958, https://doi.org/10.1016/j.mtla.2023.101958.

[41] D. Raabe, Recovery and Recrystallization: Phenomena, Physics, Models, Simulation. Physical Metallurgy, Elsevier, 2014, pp. 2291–2397.

[42] O. Messé, R. Muñoz-Moreno, T. Illston, S. Baker, H.J. Stone, Metastable carbides and their impact on recrystallisation in IN738LC processed by selective laser melting, Addit. Manuf. 22 (2018) 394–404.

[43] A. Keshavarzkermani, R. Esmaeilizadeh, P.D. Enrique, H. Asgari, N.Y. Zhou, A. Bonakdar, E. Toyserkani, Static recrystallization impact on grain structure and mechanical properties of heat-treated Hastelloy X produced via laser powder-bed fusion, Mater. Charact. 173 (2021) 110969, https://doi.org/10.1016/j.matchar.2021.110969.

[44] C.H. Yu, R.L. Peng, M. Calmunger, V. Luzin, H. Brodin, J. Moverare, Anisotropic Deformation and Fracture Mechanisms of an Additively Manufactured Ni-Based Superalloy, in: S. Tin, M. Hardy, J. Clews, J. Cormier, Q. Feng, J. Marcin, C. O'Brien, A. Suzuki (Eds.), Superalloys 2020, Springer International Publishing, Cham, 2020, pp. 1003–1013.

[45] C. Hilla, A. Wessman, R. Aman, M. Eff, R. Hayes, B. DiMarco, E. Herderik, W. Zhang, M. Mills, Effect of Solutionizing Heat Treatment on Microstructure and Mechanical Behavior of Additively Manufactured Medium Gamma Prime Nickel Superalloy, Metall. Mater. Trans. A 54 (2023) 2470–2485, https://doi.org/10.1007/s11661-023-07035-7.

[46] A. Polkowska, S. Lech, W. Polkowski, The effect of cold rolling degree on microstructure, crystallographic texture and mechanical properties of Haynes® 282® wrought nickel superalloy, Materials Science and Engineering: A 787 (2020) 139478, https://doi.org/10.1016/j.msea.2020.139478.

[47] B. Geddes, H. Leon, X. Huang, Superalloys: Alloying and Performance, ASM International, Materials Park Ohio, 2010.

[48] D. Deng, R.L. Peng, H. Brodin, J. Moverare, Microstructure and mechanical properties of Inconel 718 produced by selective laser melting: Sample orientation dependence and effects of post heat treatments, Mater. Sci. Eng., A 713 (2018) 294–306, https://doi.org/10.1016/j.msea.2017.12.043.

[49] P.K. Venkiteswaran, D.M.R. Taplin, The Creep Fracture of Inconel X-750 at 700°C, Metal Science 8 (1974) 97–106, https://doi.org/10.1179/msc.1974.8.1.97.

[50] M.R.G. Prasad, A. Biswas, N. Vajragupta, A. Hartmaier, Identification of texture characteristics for improved creep behavior of a L-PBF fabricated IN738 alloy through micromechanical simulations, Modelling Simul. Mater. Sci. Eng. 30 (2022) 55007, https://doi.org/10.1088/1361-651X/ac6e7a.

[51] M. Lapera, D. Spader, H. Ghonem, A coupled, physics-based matrix-grain boundary model for creep of carbide strengthened nickel-based superalloys - I. Concepts and formulation, Mater. Sci. Eng. A 769 (2020) 138421, https://doi.org/10.1016/j.msea.2019.138421.

[52] V. Thaveeprungsriporn, G.S. Was, The role of coincidence-site-lattice boundaries in creep of Ni-16Cr-9Fe at 360°C, Metall Mater Trans A 28 (1997) 2101–2112, https://doi.org/10.1007/s11661-997-0167-6.

[53] B. Alexandreanu, B.H. Sencer, V. Thaveeprungsriporn, G.S. Was, The effect of grain boundary character distribution on the high temperature deformation behavior of Ni–16Cr–9Fe alloys, Acta. Mater. 51 (2003) 3831–3848, https://doi.org/10.1016/S1359-6454(03)00207-6.

[54] I. Nandi, N. Ahmad, W.G. Tilson, J. Wang, N. Shamsaei, S. Shao, Crystal plasticity finite element study of tension-induced anisotropic contraction of additively manufactured Haynes 282, J. Mater. Sci. https://doi.org/10.1007/s10853-023-09076-0.